Supplementary Information for

Knowledge-informed graph attention networks enable defect-free alloy design for laser additive manufacturing

Jiabo Fu [a,#], Hao Yu [a,#], Chenchong Wang [a,*], Lingyu Wang [a], Zhongji Sun [b,*], Jinguo Li [c], Sybrand van der Zwaag [d], Dierk Raabe [e], Wei Xu [a,*]

[a] State Key Laboratory of Digital Steel, Northeastern University, Shenyang 110819, China

[b] Institute of Materials Research and Engineering (IMRE), Agency for Science, Technology and Research (A*STAR), 2 Fusionopolis Way, Innovis #08-03, Singapore 138634, Republic of Singapore

[c] Institute of Metal Research, Chinese Academy of Sciences, Shenyang 110016, China

[d] Novel Aerospace Materials Group, Faculty of Aerospace Engineering, Delft University of Technology, 2629 HS, Delft, the Netherlands

[e] Max Planck Institute for Sustainable Materials, 40237 Düsseldorf, Germany

# These authors contributed equally: Jiabo Fu, Hao Yu.

*Corresponding authors: Chenchong Wang, Email: wangchenchong@ral.neu.edu.cn

Zhongji Sun, Email: zhongji-sun@outlook.com

Wei Xu, Email: xuwei@ral.neu.edu.cn

Note that this file includes:

Supplementary Note 1: The global overview of the compositions, processing parameters, property features and defect area fraction ranges.

Supplementary Table 1. Input and output ranges of the various parameters in the database.

	Inputs and outputs	Minimum	Maximum	Mean	Standard deviation
Inputs	Nickel (wt.%)	61.8	69.08	66.41	2.75
	Aluminum (wt.%)	3.49	6.44	5.51	1.11
	Cobalt (wt.%)	8	14.6	12.26	2.77
	Chromium (wt.%)	5.05	15.93	7.90	3.76
	Molybdenum (wt.%)	0.03	2	0.62	0.85
	Tantalum (wt.%)	0.66	5	1.56	1.48
	Titanium (wt.%)	0.01	3.28	0.72	1.20
	Tungsten (wt.%)	2.25	8	3.81	1.98
	Carbon (wt.%)	0.06	0.21	0.17	0.05
	Boron (wt.%)	0.01	0.06	0.02	0.02
	Niobium (wt.%)	0	2.1	1.01	0.91
	Hafnium (wt.%)	0	0.03	0.00	0.01
	Speed (mm s^{-1})	4	14	9.94	2.76
	Power (W)	600	1600	1212.68	235.23
	Volumetric energy density (J mm^{-3})	81.25	280.80	147.24	38.37
	Hardness (HV)	367.11	485.38	420.45	32.81
Output	Defects (%)	0.05	2.51	0.79	0.66

Supplementary Table 2. Compositions (wt.%) of the five Ni-based superalloys in dataset.

Alloys	Ni	Al	Co	Cr	Mo	Ta	Ti	W	C	B	Nb	Hf	Printability
AMS-OR	Bal.	5.83	14.1	7.28	0.03	0.66	0.01	2.25	0.21	0.02	2.1	-	Easy-to-print
IN738	Bal.	3.49	8.41	15.93	1.76	1.74	3.28	2.63	0.14	0.01	0.81	-	Hard-to-print
AMS-mCB	Bal.	4.5	8	8	2	5	1	8	0.06	0.06	-	0.03	Hard-to-print
AMSC-DB	Bal.	6.24	14.6	5.95	0.03	0.97	0.03	2.25	0.2	0.01	2.1	-	Easy-to-print
AMS-nDB	Bal.	6.44	13.8	5.05	0.06	0.67	0.03	4.48	0.2	0.02	0.17	-	Hard-to-print

As shown in Supplementary Table 2, the experimentally established dataset of 142 samples encompasses five distinct alloy compositions, including the printable alloys AMSC-DB and AMS-OR and the hard-to-print, crack-prone alloys AMS-nDB, AMS-mCB, and IN738. The compositional ranges of these samples cover approximately 75% of the reported composition space for Ni-based superalloys, as illustrated in Supplementary Fig. 1a. Regarding the processing parameters, we have exhaustively explored the feasible ranges of laser speed and power achievable with the equipment used, resulting in a randomized variation across the parameter space (Supplementary Fig. 1b).

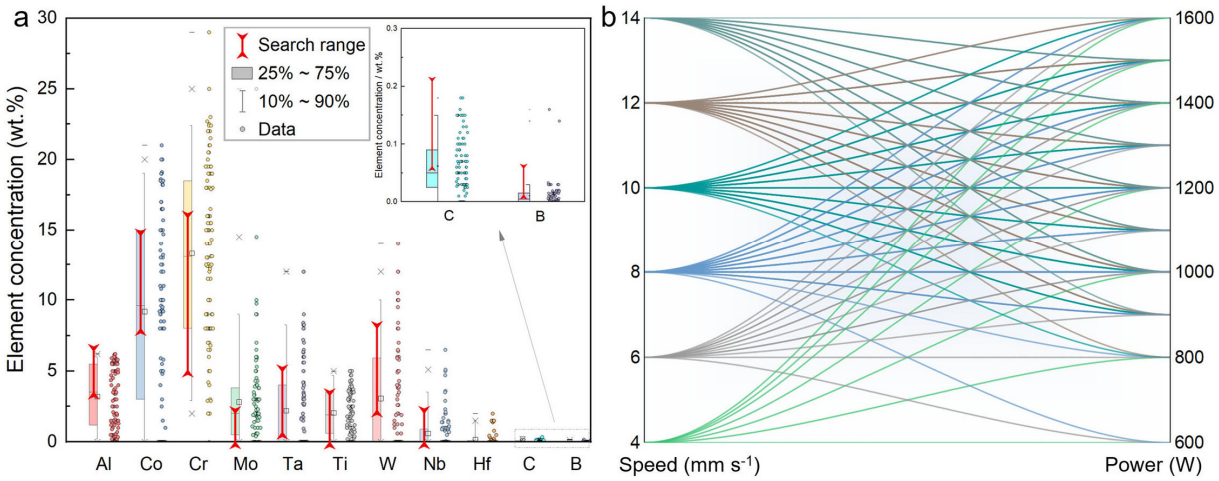

Supplementary Figure 1. Composition and processing-parameter ranges for the Ni-superalloy dataset. **a** Distribution of alloying-element concentrations for existing Ni superalloys[1] (n = 101), and the search ranges for elements in this work. **b** Distribution of processing parameters in dataset (n = 142 samples from five Ni-based superalloys). Colors and shaded ranges are defined in the panels. Error bars and inferential statistical tests are not applicable to these range and distribution plots.

Supplementary Note 2: Histograms of the mechanistic variables and thermodynamic variables.

Supplementary Figure 2a-d displays histograms depicting the ranges of mechanistic variables in the dataset used. The grain morphology of metals during the L-DED process is dependent on solidification parameters. One such parameter is the temperature gradient (G), which acts normal to the solidification front. The model presented in this paper is based on the Cartesian coordinate system, and G is expressed as:

$$G = \left(\frac{\partial T}{\partial x}, \frac{\partial T}{\partial y}, \frac{\partial T}{\partial z}\right) \tag{S1}$$

Growth velocity R is another solidification parameter which is normal to the solid/liquid interface and its magnitude can be expressed as[2]:

$$R = v_{\mathrm{s}} \cdot \frac{\frac{\partial T}{\partial x}}{G} \tag{S2}$$

The solidification parameter $G \cdot R$ is related to the grain size, representing the instantaneous cooling rate on the solidification front. The ratio of G/R is the solidification parameter ε, which has important relevance to the microstructural morphology[3-5].

Supplementary Figure 2e-h shows the histograms of the ranges of thermodynamic variables in the dataset used. Using Thermo-Calc software based on TCNI 12 and MOBNI 6 database, thermodynamic variables closely related to alloy composition were quantitatively simulated. In a single-track simulation, the average temperature at the midpoint, recorded after the laser heat source has passed and the temperature has decreased to the γ′ solvus temperature, is used as the basis for thermodynamic calculations. The variables include: the effective diffusion coefficient, D_{L} (expressed as Eq. (S3)[6-8]); the compositional concentration difference between the g matrix phase and the γ′ phase, $X_{\mathrm{i}}^{\mathrm{m-p}}$ (expressed as Eq. (S4)[6]); the molar volume of the γ′ phase[4,9], $V_{\mathrm{m}}^{\mathrm{p}}$ and the driving force of γ′ phase $D_{\mathrm{f}}^{\mathrm{p}}$ (directly obtained from Thermo-Calc software). These simulations were conducted to evaluate the crack susceptibility caused by the precipitation and coarsening of the γ′ phase during additive manufacturing.

$$D_{\mathrm{L}} = \sum_{i=1}^{n} x_{\mathrm{i}}^{\mathrm{mp}} \cdot D_{\mathrm{i}} \tag{S3}$$

$$X_{\mathrm{i}}^{\mathrm{m-p}} = \sum_{i=1}^{n} \left(x_{\mathrm{i}}^{\mathrm{p}} - x_{\mathrm{i}}^{\mathrm{mp}}\right)^2 \tag{S4}$$

where $x_{\mathrm{i}}^{\mathrm{p}}$ and $x_{\mathrm{i}}^{\mathrm{mp}}$ is the concentration of element i in γ′ phase and γ matrix respectively, and D_{i} is the diffusion coefficient of element i in γ matrix during additive manufacturing. The relevant temperature is captured by simulation of single-track printing.

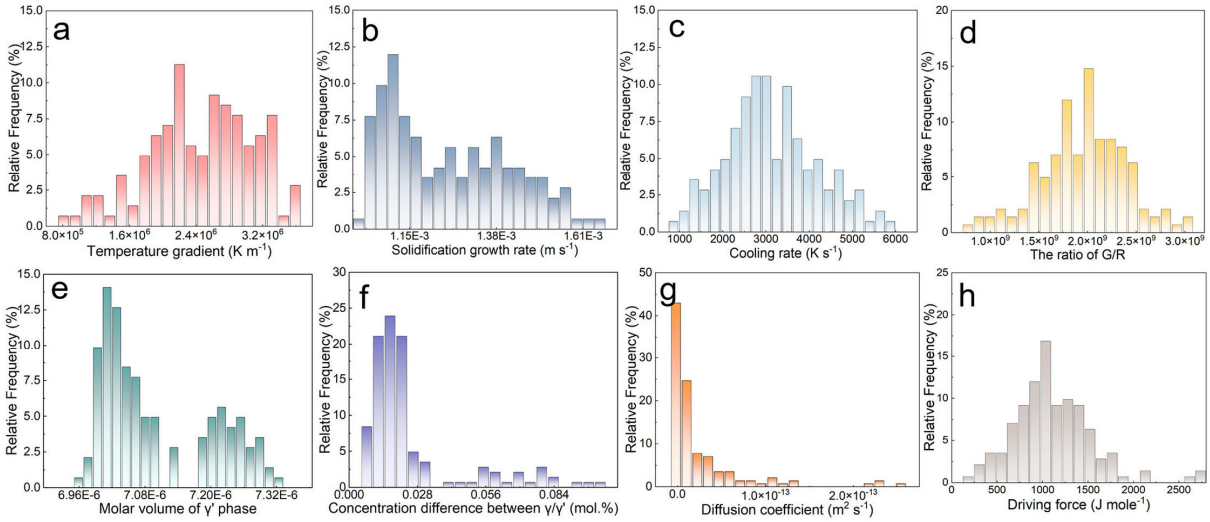

Supplementary Figure 2. Distribution histograms of mechanistic and thermodynamic variables in the Ni-superalloy dataset. a Temperature gradient. **b** Solidification growth rate. **c** Cooling rate. **d** Ratio of *G/R*. **e** Molar volume of γ′ phase. **f** Concentration difference between γ/γ′. **g** Diffusion coefficient. **h** Driving force of γ′ phase. Histograms summarize the dataset used for model construction (n = 142 samples). Bars indicate the distribution of calculated or simulated values.

Supplementary Note 3: Prediction of mechanistic variables, thermodynamic variables and property features based on CNN model.

For the reverse design process of alloy compositions and processing parameters, integrating the UQ-KGAT model with the genetic algorithm NSGA-II is crucial. Prior to designing alloys, it is essential to establish quantitative correlations between composition-process and thermodynamic variables, solidification mechanistic variables, as well as between composition-process, thermodynamic variables, solidification mechanistic variables, and volumetric energy density and hardness, using machine learning algorithms. These characteristics reflect the mathematical and physical relationships between composition-process and physical metallurgical variables. As a result, features identified through these computational and simulation methods are often of high quality. In this study, a convolutional neural network algorithm was employed to establish the relationship between input and output features. The applicability of CNN has been verified in other studies[10,11], where CNN has demonstrated superior performance compared to traditional neural networks. The optimal model prediction results for solidification mechanistic variables and thermodynamic variables are shown in Supplementary Fig. 3a-f. The results indicate that the CNN model's R^2 values for both the training set and test set exceed 95%, and it also achieves a low mean absolute error (MAE). Thus, the quantitative correlation between composition-process and physical metallurgical variables established using the CNN model has high predictive accuracy and excellent generalization ability.

Similarly, a quantitative correlation between composition, process, physical metallurgical variables, and property variables was established using the CNN model. The parameters of the convolutional neural network were set as follows: the first convolutional layer is 5×5×8, the second convolutional layer is 5×5×16, the fully connected layer is 1×1×256, and the filter size is 3×3. For CNN training, the model was obtained after 1600 iterations, using a mean-squared error loss function, a learning rate of 0.001, and the Adam optimizer. The prediction results of the optimal model under 20 random divisions are shown in Supplementary Fig. 3g and h. Unlike the prediction of defect levels by machine learning models, the CNN models accurately predict volumetric energy density and hardness. For volumetric energy density, the R^2 value on the test set is 97.3%, with an MAE of only 5.29 J mm^{-3}. For hardness, the R^2 value on the test set is 94.96%, with an MAE of 7.03 HV. The high accuracy is primarily because, compared to defect measurements, the property characteristics of alloys can often be measured more precisely using existing experimental methods, resulting in lower data noise and higher data quality.

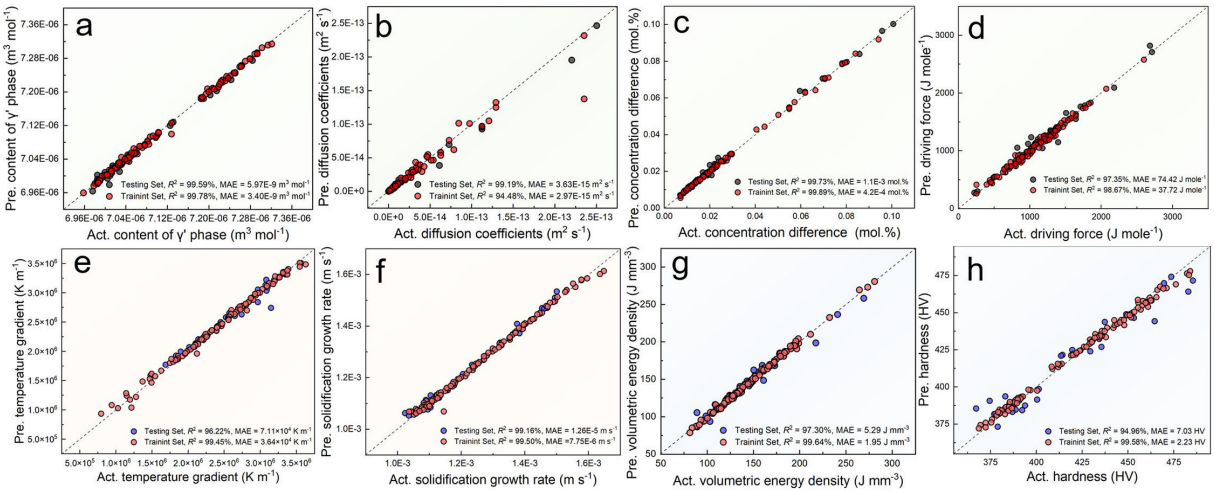

Supplementary Figure 3. CNN-based prediction of intermediate variables. a Molar volume of γ′ phase. **b** Diffusion coefficients. **c** Concentration difference between γ/γ′. **d** Driving force. **e** Temperature gradient. **f** Solidification growth rate. **g** Volumetric energy density. **h** Hardness. The models were trained and evaluated on the Ni-superalloy dataset (n = 142 samples), with training/testing partitions and R^2/MAE metrics indicated in the panels, and the optimal model was selected from 20 random data splits.

Supplementary Note 4: Prediction of defect area fraction via different machine learning models.

In this study, the defect prediction performance of various machine learning models for the AM-ed Ni-based superalloys was compared. These models include Gradient Boosting Regression (GBR), Gaussian Process Regression (GPR), Multilayer Perceptron (MLP), Random Forest (RF), Support Vector Regression with a radial basis function kernel (SVR), and Extreme Gradient Boosting (XGB). Model parameters were optimized using the grid search method. Additionally, deep learning models, such as the Convolutional Neural Network (CNN) and the Knowledge-informed Graph Attention Network (KGAT), along with our proposed Uncertainty-Quantified Knowledge-informed Graph Attention network (UQ-KGAT), were also used for comparison. The average R^2 and MAE values under 20 random divisions are shown in Supplementary Fig. 5a and b. The results indicate that due to the high noise in the defect data, various machine learning models struggle to achieve accurate predictions.

	Al	Co	Cr	Mo	Ta	Ti	W	C	B	Nb	Hf	Speed	Power	D_f^p	D_L	X_i^{m-p}	V_m	R	G	τ	ε	E_v	Hardness
Al	0	0	0	0	0	0	0	0	0	0	0	0	0	1	1	1	1	1	1	1	1	1	1
Co	0	0	0	0	0	0	0	0	0	0	0	0	0	1	1	1	1	1	1	1	1	1	1
Cr	0	0	0	0	0	0	0	0	0	0	0	0	0	1	1	1	1	1	1	1	1	1	1
Mo	0	0	0	0	0	0	0	0	0	0	0	0	0	1	1	1	1	1	1	1	1	1	1
Ta	0	0	0	0	0	0	0	0	0	0	0	0	0	1	1	1	1	1	1	1	1	1	1
Ti	0	0	0	0	0	0	0	0	0	0	0	0	0	1	1	1	1	1	1	1	1	1	1
W	0	0	0	0	0	0	0	0	0	0	0	0	0	1	1	1	1	1	1	1	1	1	1
C	0	0	0	0	0	0	0	0	0	0	0	0	0	1	1	1	1	1	1	1	1	1	1
B	0	0	0	0	0	0	0	0	0	0	0	0	0	1	1	1	1	1	1	1	1	1	1
Nb	0	0	0	0	0	0	0	0	0	0	0	0	0	1	1	1	1	1	1	1	1	1	1
Hf	0	0	0	0	0	0	0	0	0	0	0	0	0	1	1	1	1	1	1	1	1	1	1
Speed	0	0	0	0	0	0	0	0	0	0	0	0	0	1	1	1	1	1	1	1	1	1	1
Power	0	0	0	0	0	0	0	0	0	0	0	0	0	1	1	1	1	1	1	1	1	1	1
D_f^p	0	0	0	0	0	0	0	0	0	0	0	0	0	0	0	0	0	0	0	0	0	0	1
D_L	0	0	0	0	0	0	0	0	0	0	0	0	0	0	0	0	0	0	0	0	0	0	1
X_i^{m-p}	0	0	0	0	0	0	0	0	0	0	0	0	0	0	0	0	0	0	0	0	0	0	1
V_m	0	0	0	0	0	0	0	0	0	0	0	0	0	0	0	0	0	0	0	0	0	0	1
R	0	0	0	0	0	0	0	0	0	0	0	0	0	0	0	0	0	0	0	1	1	1	1
G	0	0	0	0	0	0	0	0	0	0	0	0	0	0	0	0	0	0	0	1	1	1	1
τ	0	0	0	0	0	0	0	0	0	0	0	0	0	0	0	0	0	0	0	0	0	1	1
ε	0	0	0	0	0	0	0	0	0	0	0	0	0	0	0	0	0	0	0	0	0	1	1
E_v	0	0	0	0	0	0	0	0	0	0	0	0	0	0	0	0	0	0	0	0	0	0	1
Hardness	0	0	0	0	0	0	0	0	0	0	0	0	0	0	0	0	0	0	0	0	0	0	0

Supplementary Figure 4. Adjacency matrix of physical-metallurgy knowledge graph. Rows and columns correspond to composition elements, processing parameters, thermodynamic variables, mechanistic variables and property features. Matrix entries of 1 indicate an edge included in the graph, whereas entries of 0 indicate no direct graph connection. The shaded row and column headers group related node types.

Among the models evaluated, the KGAT model, which incorporates a physical metallurgy knowledge graph, achieved an average R^2 of 75.1% and an average MAE of 0.2440% over 20 random data splits. With the integration of uncertainty quantification, the proposed UQ-KGAT model demonstrated improved performance, with R^2 increasing to 76.7% and MAE decreasing to 0.2384%, accompanied by a narrower error interval, indicating enhanced predictive stability. As shown in Supplementary Fig. 5c and d, the best-performing instances of both KGAT and UQ-KGAT across the 20 splits achieved R^2 values exceeding 80%, suggesting generally sound prediction capability. However, a sample-wise analysis reveals distinct behavioral differences: the predictions for low-defect samples are relatively accurate, and all models exhibit considerable deviations for high-defect samples. The scatter of data points away from the 1:1 line underscores the potential risks of directly applying these models to the inverse design of alloy compositions and processing parameters. In contrast, the proposed UQ-KGAT model provides not only point predictions but also quantifies the associated uncertainty. This enriched predictive information is critical for supporting a more rational and reliable inverse design strategy for alloys, as it enables explicit consideration of prediction confidence during the optimization process.

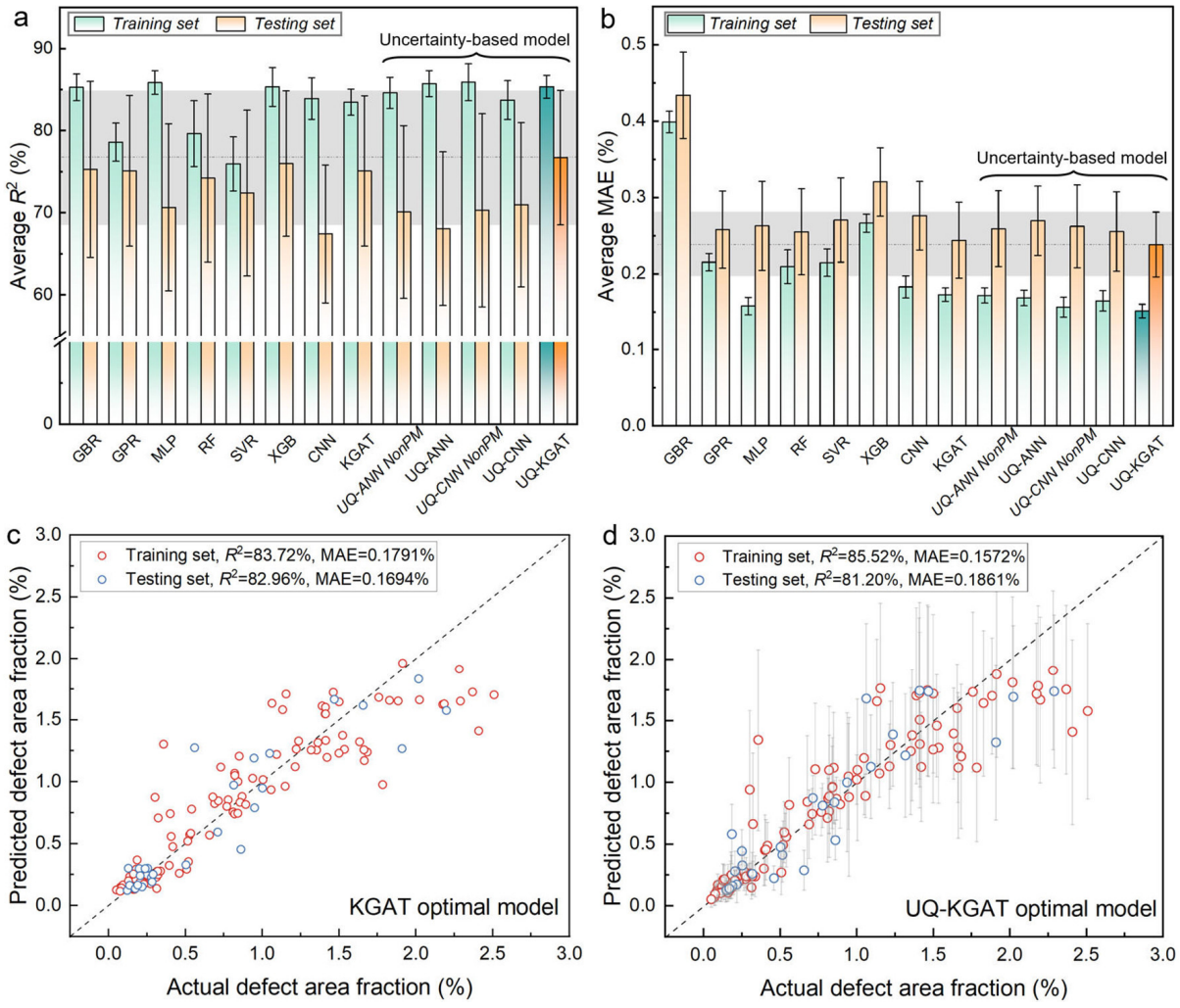

Supplementary Figure 5. Performance of different machine learning models for defect-area-fraction

prediction. a Average R^2 for the training and testing sets. **b** Average MAE for the training and testing sets. **c** Best KGAT result among 20 random partitions. **d** Best UQ-KGAT result among 20 random partitions. The Ni-superalloy dataset contains $n = 142$ samples and was evaluated using 20 random training/testing partitions; green and orange bars indicate training and testing sets, respectively. The dashed line in **c** and **d** is the ideal 1:1 prediction line, red and blue points denote training and testing samples, and grey error bars in **d** indicate the UQ-KGAT prediction uncertainty.

Supplementary Note 5: Design process of alloy composition and AM process using ML models and NSGA-II.

For the genetic algorithm NSGA-II, an initial population must be generated within specific composition and process intervals. In this study, these intervals are determined based on the maximum and minimum values recorded in the raw data (see Supplementary Table 1). After initializing the composition and process, the corresponding hierarchical relationships between composition/process, thermodynamic variables, solidification mechanistic variables, and property variables are established using the optimal CNN models, thereby constructing a physical metallurgy knowledge graph. The graph structure is then used as the input for the UQ-KGAT model, which predicts the defect level and uncertainty level of these samples. This approach enables the reverse search and design optimization process of alloy composition and process[12].

The models in this research are all based on the PyTorch framework in Python. The architectural settings of the UQ-KGAT model are detailed in the Supplementary Table 3, in which the hidden layer vector of graph attention is set to 2, utilizing a two-head attention mechanism. A learning rate of 0.0008 is selected, and iterative training of the neural network is conducted using the Adam optimizer combined with the CosineAnnealingLR decay strategy. Training is randomly divided 20 times to identify the optimal model, with both the training set and test set achieving an R^2 greater than 80%, for subsequent alloy design. The population size for the genetic algorithm NSGA-II is set to 50, with a maximum of 1500 iterations, a crossover probability of 0.9, and a mutation probability of 0.2.

Supplementary Table 3. The UQ-KGAT architecture details.

Layer(type)	Shape
GraphAttentionLayer (graph_modules)	23
flatten_1 (Flatten)	92
dense_1 (Dense)	128
relu_1 (Relu)	128
dropout_1 (Dropout)	128
dense_2 (Dense)	16
dense_2 (Gelu)	16
dense_4 (Dense)	2

Supplementary Note 6: Effects of uncertainty strategies and training data size on defect prediction and alloy design.

Supplementary Figure 6 shows the prediction and design of defects and uncertainty by KGAT models with different types of uncertainty. As shown in Supplementary Fig. 6a and b, the proportion of statistical uncertainty was found to be higher compared to model uncertainty. To compare the role of different types of uncertainties in the design process, the reverse design of alloy was carried out using the SQ-KGAT model (Statistical Uncertainty-quantified KGAT model) and the MQ-KGAT model (Model Uncertainty-quantified KGAT model), as detailed in Supplementary Fig. 6c and d. When reverse design is performed with defect area fraction as the sole objective, the designed alloy exhibits high model uncertainty. When reverse design is performed with statistical uncertainty and defect area fraction as dual objectives, the designed alloy exhibits lower statistical uncertainty and lower defect levels, but higher model uncertainty. When the reverse design is based on model uncertainty and defect area fraction as dual objectives, although the designed alloy exhibits lower model uncertainty, the predicted defect levels are not improved compared to the original defect levels in the dataset.

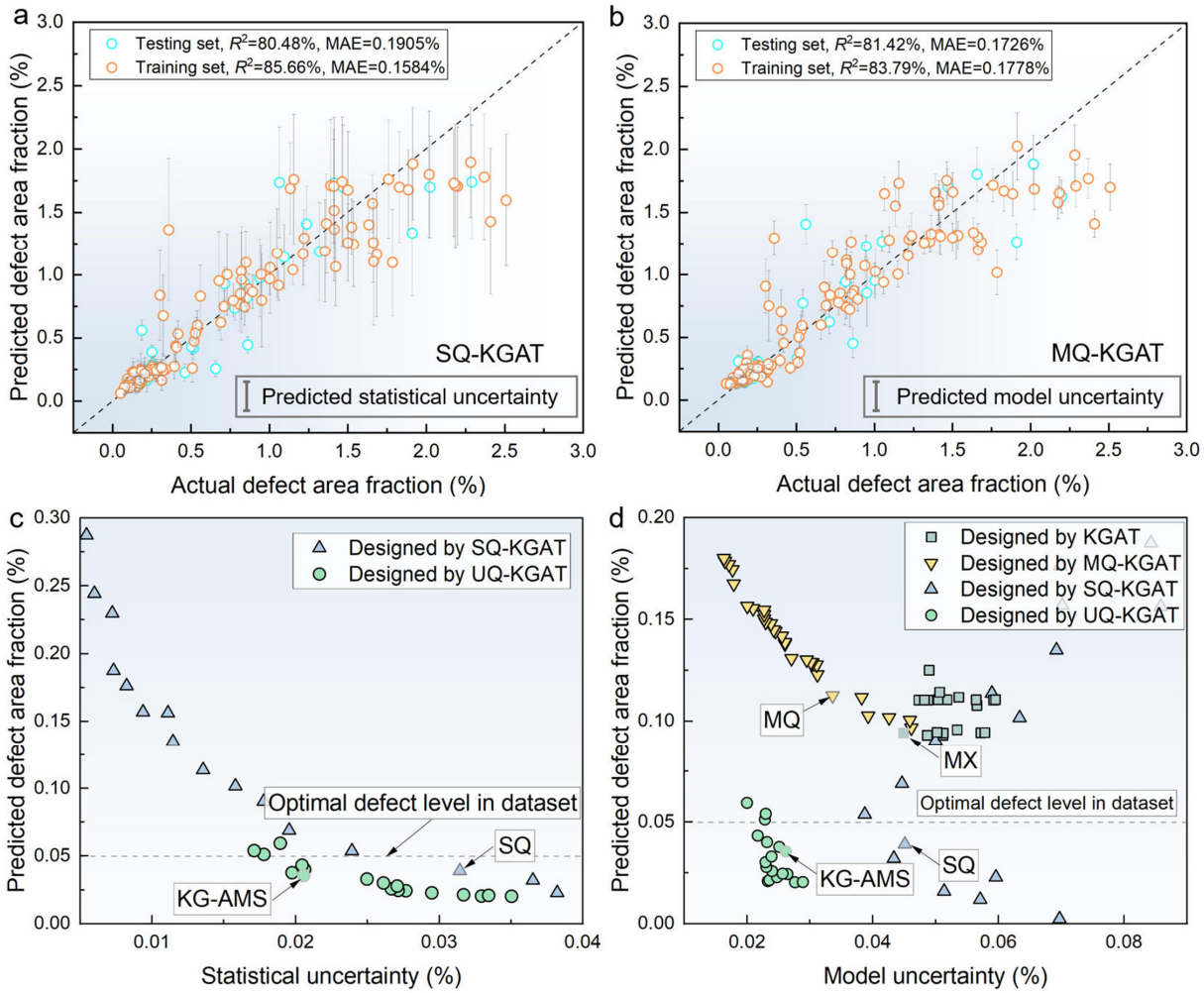

Supplementary Figure 6. Defect prediction and inverse design using KGAT models with different

uncertainty quantification strategies. a Prediction results of the Statistical Uncertainty-quantified KGAT (SQ-KGAT) model. **b** Prediction results of the Model Uncertainty-quantified KGAT (MQ-KGAT) model. **c** Design results based on SQ-KGAT versus the proposed UQ-KGAT model. **d** Comparison of design results from KGAT, MQ-KGAT, SQ-KGAT, and UQ-KGAT. Prediction panels are based on the Ni-superalloy dataset (n = 142 samples), axes, markers and uncertainty quantities are defined in the panels.

To further investigate the impact of training data size on model extrapolation capability, we excluded one alloy AMS-mCB from our original dataset. This reduced the number of training samples from 142 to 121 and, more importantly, intentionally narrowed the compositional ranges for several key elements, as illustrated in Supplementary Fig. 7a. The red bars represent the original ranges from the 142-sample set, while the black bars show the substantially reduced ranges from the 121-sample set. Notably, the ranges were narrowed for: Ta (from 0.66–5 wt.% to 0.66–1.74 wt.%), W (from 2.25–8 wt.% to 2.25–4.48 wt.%), C (from 0.06–0.21 wt.% to 0.14–0.21 wt.%), and B (from 0.01–0.06 wt.% to 0.01–0.02 wt.%), all of which are known to significantly influence the printability and mechanical properties of Ni-based superalloys[13].

Supplementary Table 4. Compositions (in wt.%) and processing parameters designed using different ML models.

Alloys	Al	Co	Cr	Mo	Ta	Ti	W	C	B	Nb	Hf	Ni	Power	Speed
SQ	6.44	15.59	5.05	0.49	3.18	0.13	4.12	0.21	0.01	2.09	0.01	Bal.	1500	8
MQ	6.35	11.2	7.87	1.96	2.13	1.62	3.01	0.19	0.01	1.93	0.01	Bal.	1200	10
MX	6.34	14.6	7.01	0.67	1.74	0.39	5.54	0.18	0.01	1.27	0.02	Bal.	1600	9
KG-AMS	6.31	14.59	5.06	0.25	1.56	0.14	2.25	0.21	0.01	2.10	0.006	Bal.	1500	10
Alloy 1	6.44	12.91	15.84	1.18	3.88	0.11	2.83	0.06	0.01	1.85	0.02	Bal.	1540	11
Alloy 2	6.43	13.63	13.45	0.31	0.86	1.79	7.45	0.21	0.01	2.06	0	Bal.	1560	6
Alloy 3	6.39	14.6	5.09	1.27	4.99	0.13	2.41	0.21	0.01	2.1	0.03	Bal.	1070	4
Alloy 4	5.85	8	12.78	2	2.29	3.27	3.25	0.14	0.01	0.72	0.01	Bal.	1560	4

A model trained solely on this restricted dataset (4 alloy variants) still demonstrated good predictive accuracy, as shown in Supplementary Fig. 7b. The design results are presented in Supplementary Fig. 7c. It is important to note that the design space here remains the original, broader composition ranges (represented by the red bars in Supplementary Fig. 7a) rather than the narrowed training ranges. As expected, the Pareto front identified using this smaller dataset exhibits higher uncertainty. Crucially, however, the framework still successfully identified an "optimal" alloy, designated as Alloy D1, with a predicted defect area fraction below 0.05%. The compositional difference between Alloy D1 and the originally designed KG-AMS alloy is minimal, as detailed in Supplementary Fig. 7d, with only slight variations in Al (6.31 vs. 6.39 wt.%), Ta (1.56 vs. 1.64 wt.%), and C (0.21 vs. 0.20 wt.%). The results indicate that our model demonstrates robust performance and converges on a similar optimal compositional region even when trained on a more limited and narrower dataset. This strengthens our confidence in the reliability of the identified design, suggesting it

is not an artifact of a specific dataset configuration but a robust outcome of the underlying process-structure-property relationships captured by the model.

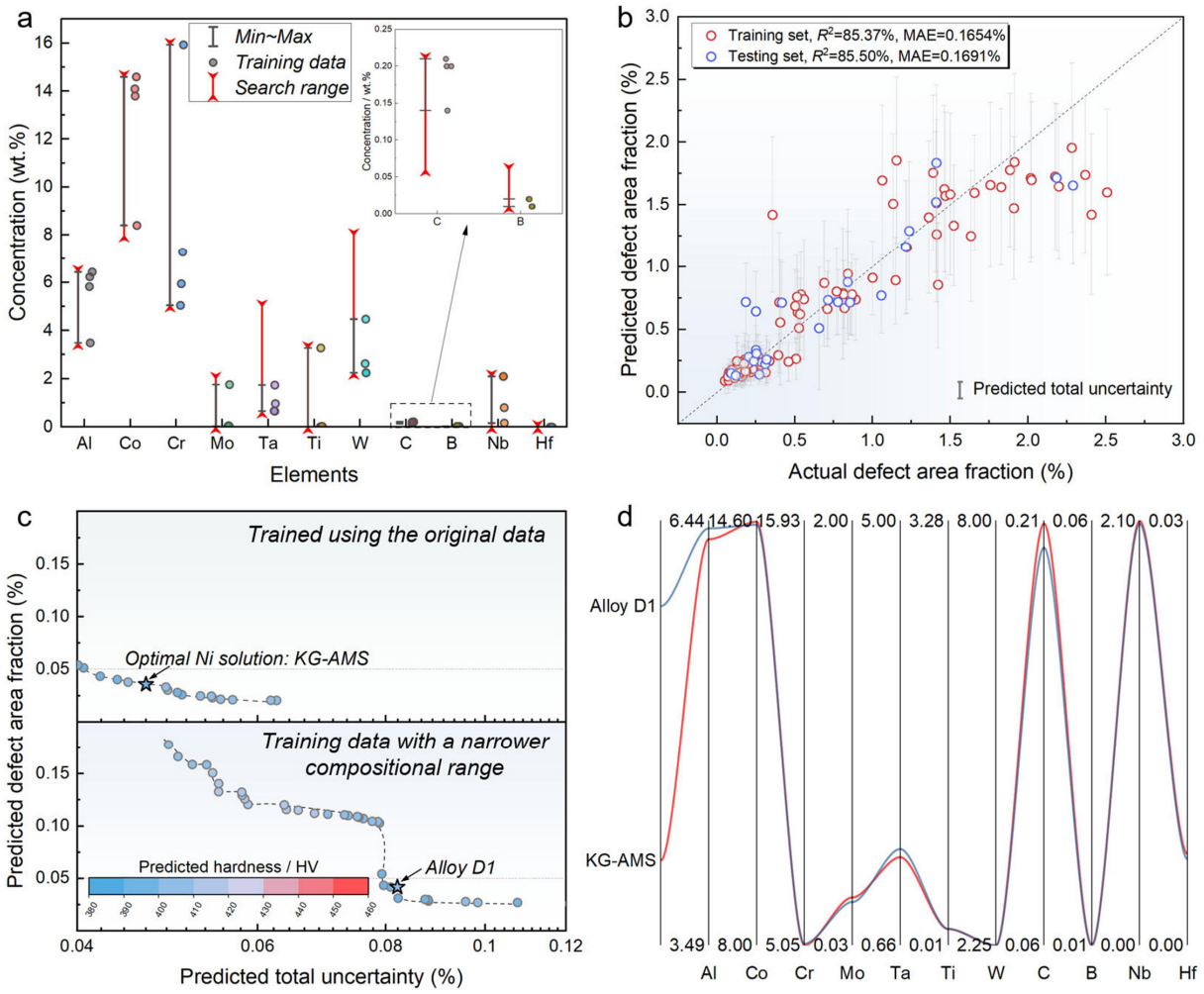

Supplementary Figure 7. Model validation with a restricted training dataset. a Elemental ranges in the original 142-sample dataset and in the restricted 121-sample dataset after excluding AMS-mCB. **b** Predictive performance of the model trained on the restricted dataset. **c** Pareto front and selected optimal Alloy D1. **d** Compositional comparison between Alloy D1 and KG-AMS. Red and black bars in **a** denote the original and restricted composition ranges, respectively; the broader original ranges were retained as the inverse-design space.

Smaller deviations from the target chemical composition are inevitable in industrial production. Therefore, compositional robustness of the optimal alloy formulation is a critical yet unresolved aspect in model-based alloy design. An alloy composition is considered robust if variations within the allowable compositional range do not result in a significant increase in predicted defect levels[14]. To investigate the compositional robustness of the optimal formulation, we defined the compositional fluctuation ranges for each relevant chemical element in alloy KG-AMS: Al ±0.5 wt.%, Co ±0.5 wt.%, Cr ±0.5 wt.%, Mo ±0.1 wt.%, Ta ±0.5 wt.%, Ti ±0.05 wt.%, W ±0.5 wt.%, C ±0.05 wt.%, Nb ±0.5 wt.%, and Hf ±0.005 wt.%. The results are shown

in Supplementary Fig. 8, with the positive and negative deviations in concentration denoted as "+" and "–", respectively. It can be observed that the elements with the most significant impact on the printing performance of alloy KG-AMS are C and Nb, with the defect level within 0.08%. Overall, the composition of KG-AMS exhibits good robustness: fluctuations in most elements result in defect levels remaining below 0.05%, which is superior to the minimum defect level in the dataset.

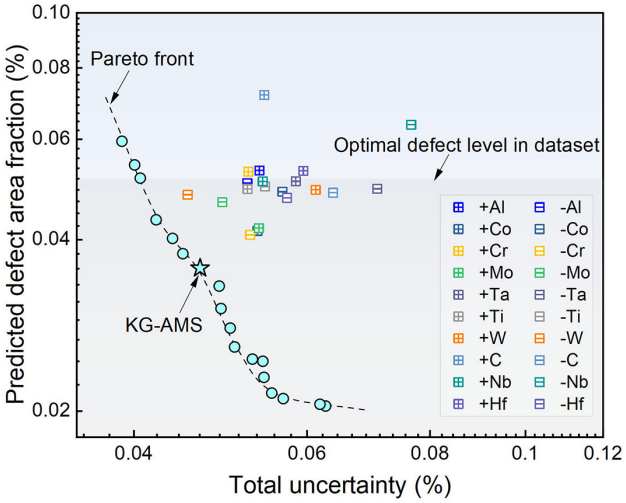

Supplementary Figure 8. Effects of compositional perturbations on predicted defect level and uncertainty for KG-AMS. The positive and negative deviations of concentrations are indicated by "+" or "–" in the symbols, respectively. The perturbation ranges were Al ±0.5 wt.%, Co ±0.5 wt.%, Cr ±0.5 wt.%, Mo ±0.1 wt.%, Ta ±0.5 wt.%, Ti ±0.05 wt.%, W ±0.5 wt.%, C ±0.05 wt.%, Nb ±0.5 wt.% and Hf ±0.005 wt.%. Each point corresponds to one compositional perturbation case.

Supplementary Note 7: Analysis of crack susceptibility and high-temperature mechanical properties using traditional thermodynamic empirical criteria.

In this study, after conducting the reverse design of alloy composition and process using various machine learning models and genetic algorithms NSGA-II, thermodynamic simulations were performed on the alloys designed by different models based on traditional empirical criteria. These simulations were aimed at evaluating the crack susceptibility and high-temperature mechanical properties of the alloys.

For the evaluation of crack susceptibility in the designed alloys, two aspects are considered: hot-crack susceptibility and strain-aging crack susceptibility. The solidification behavior of the alloy under non-equilibrium conditions is calculated and simulated using the Scheil-Gulliver model. The Freezing range criterion (FR, calculated using Eq. (S5)) is then employed to assess the hot-crack susceptibility of the alloys.

$$\mathrm{FR} = T^{\mathrm{SG}}_{\mathrm{Liquidus}} - T^{\mathrm{SG}}_{\mathrm{Solidus}} \tag{S5}$$

where $T^{\mathrm{SG}}_{\mathrm{Liquidus}}$ and $T^{\mathrm{SG}}_{\mathrm{Solidus}}$ are the liquidus and solidus temperature, respectively. To reasonably consider the effect of back diffusion for interstitial atoms, boron and carbon atoms are set as fast diffusers in Scheil-Gulliver simulation[15].

In addition, the criterion used to rank strain-age crack susceptibility (SAC factor) is based on precipitation behavior of γ' phase[16,17], where the SAC factor is calculated as the derivative of the γ volume fraction with respect to temperature:

$$\mathrm{SAC} = {dV_{\mathrm{f}}^{\gamma}}\Big/{dT}, T \in \left[T_{\gamma}^{*}, T_{\mathrm{Solidus}}\right] \tag{S6}$$

where V_{f}^{γ} represents the equilibrium volume fraction of the γ phase; T_{γ}^{*} denotes the temperature at which the phase fraction of γ matrix reaches 80% during solid-state transformation and T_{Solidus} is the equilibrium solidus temperature.

The equilibrium phase composition of the designed alloy at 900 °C was calculated using thermodynamic simulations to assess the rationality of the alloy composition design by different machine learning models. Special attention was paid to the content of the γ′ phase and other undesirable phases (excluding the γ matrix phase and γ′ precipitate phase). The presence of these phases is critical as they not only influence the microstructural stability of the alloy at high temperature but also impact its high-temperature mechanical properties and printability[17].

Supplementary Note 8: The distribution of actual defect level for alloys KG-AMS and AMS-mCB.

Supplementary Figure 9 illustrates the distribution of actual defects in KG-AMS alloy under laser power ranging from 1000 to 1500 W and a scanning speed of 8 to 12 mm s^{-1}.

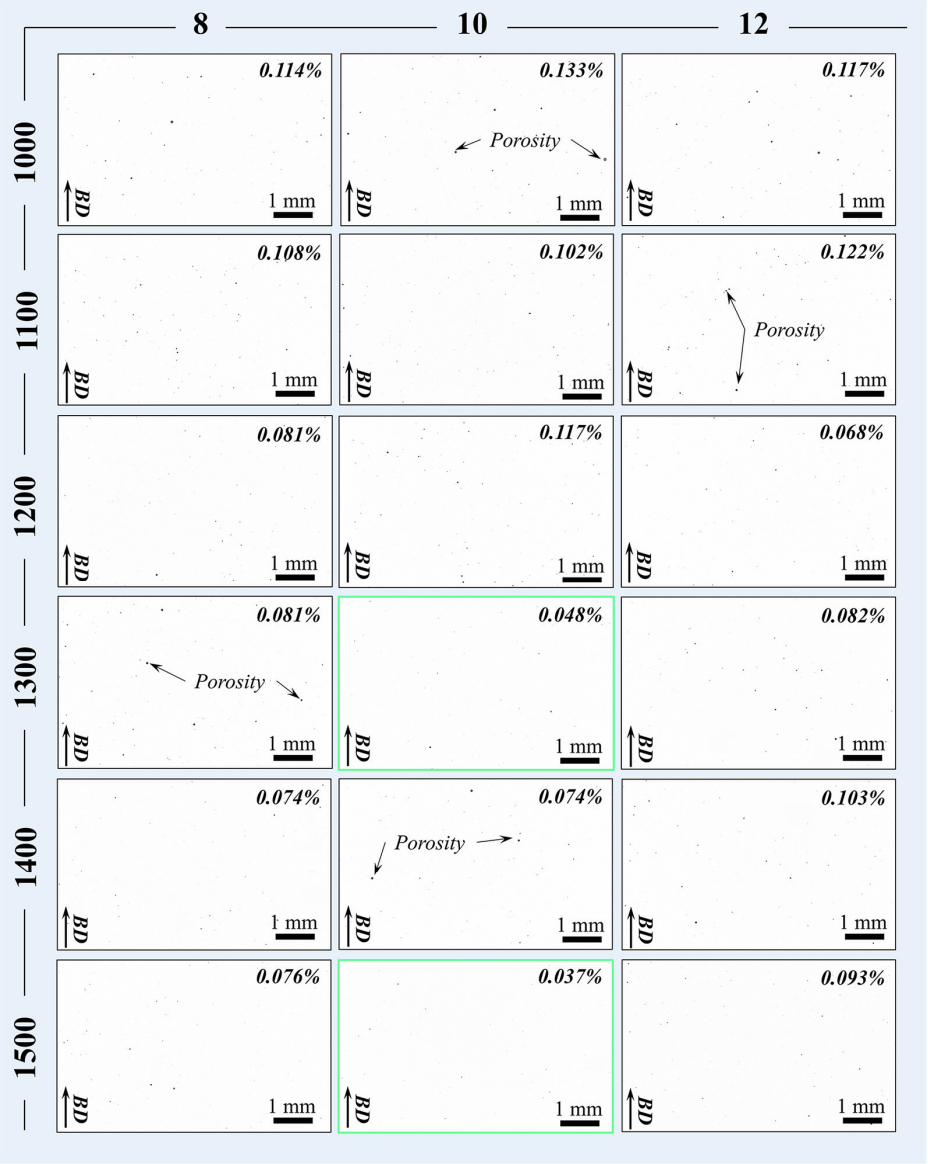

Supplementary Figure 9. Distribution of actual defects in alloy KG-AMS under different L-DED processing parameters. Rows correspond to laser power from 1000 to 1500 W and columns correspond to scanning speed from 8 to 12 mm s^{-1}. Percentages in each optical micrograph indicate the measured defect area fraction for the displayed condition. Arrows labelled BD indicate the building direction, arrows labelled porosity identify representative pores, green frames highlight low-defect parameter sets, and all scale bars are 1 mm.

Supplementary Figure 10 illustrates the distribution of actual defects in AMS-mCB alloy under laser power

ranging from 1000 to 1500 W and a scanning speed of 8 to 12 mm s^{-1}.

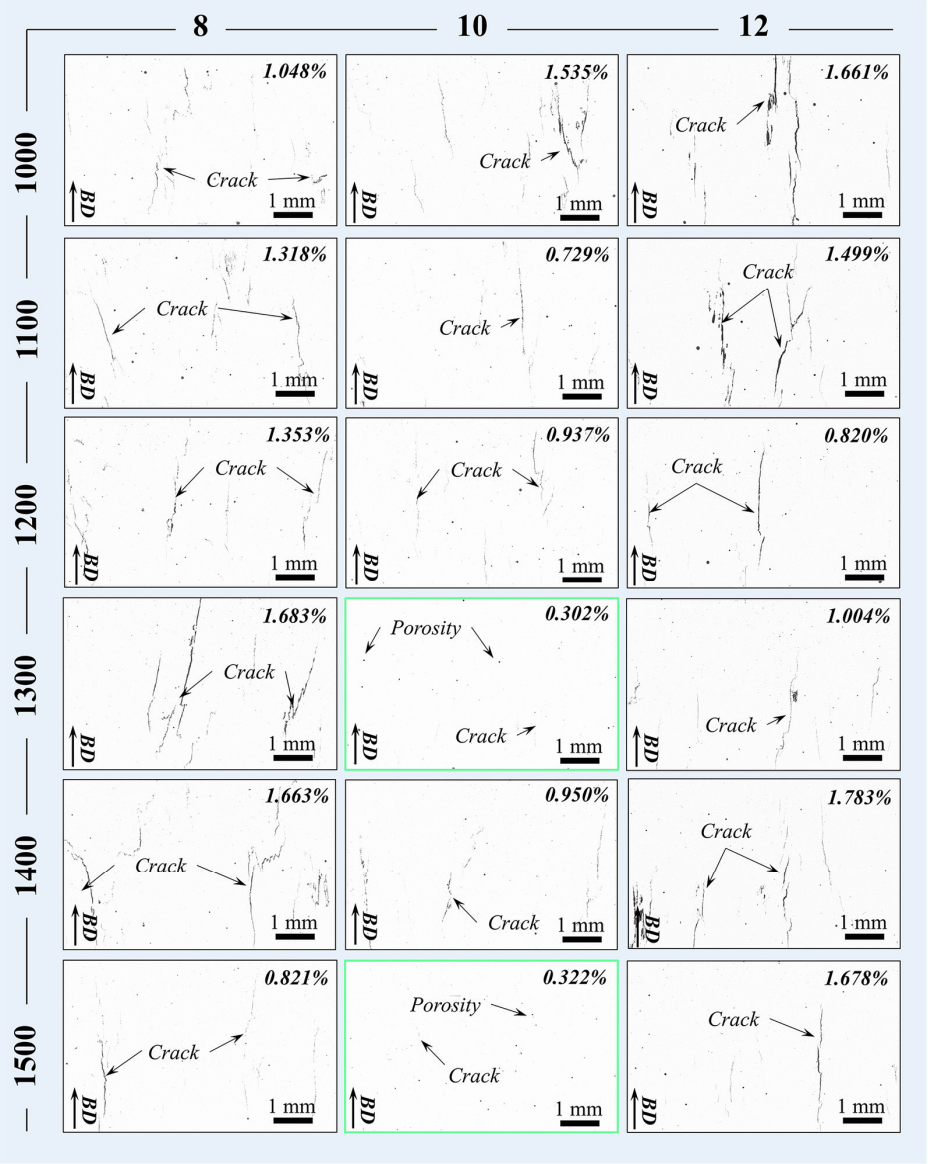

Supplementary Figure 10. Distribution of actual defects in alloy AMS-mCB under different L-DED processing parameters. Rows correspond to laser power from 1000 to 1500 W and columns correspond to scanning speed from 8 to 12 mm s^{-1}. Percentages in each optical micrograph indicate the measured defect area fraction for the displayed condition. Arrows labelled BD indicate the build direction, arrows labelled crack or porosity identify representative defects, green frames highlight relatively lower-defect parameter sets, and all scale bars are 1 mm.

High-resolution X-ray computed tomography (CT) was further performed on a sample of the designed alloy KG-AMS, which exhibited a defect area fraction of 0.037%. Two parallel samples were examined under high resolution to thoroughly detect potential cracks. As shown in Supplementary Fig. 11, subsequent 3D reconstruction confirmed the absence of any crack-like features (sphericity >0.6), revealing only isolated pores. Specifically, the equivalent pore diameters were primarily distributed between 0 and 60 μm, with a total porosity of 0.036% or 0.04% (i.e., averaging 0.038%). These results align closely with the actual defect

area fraction measured by 2D optical microscopy (0.037%) and that predicted by the UQ-KGAT model (0.036%), thereby further verifying the reliability of the OM-based defect quantification method and the proposed machine learning framework.

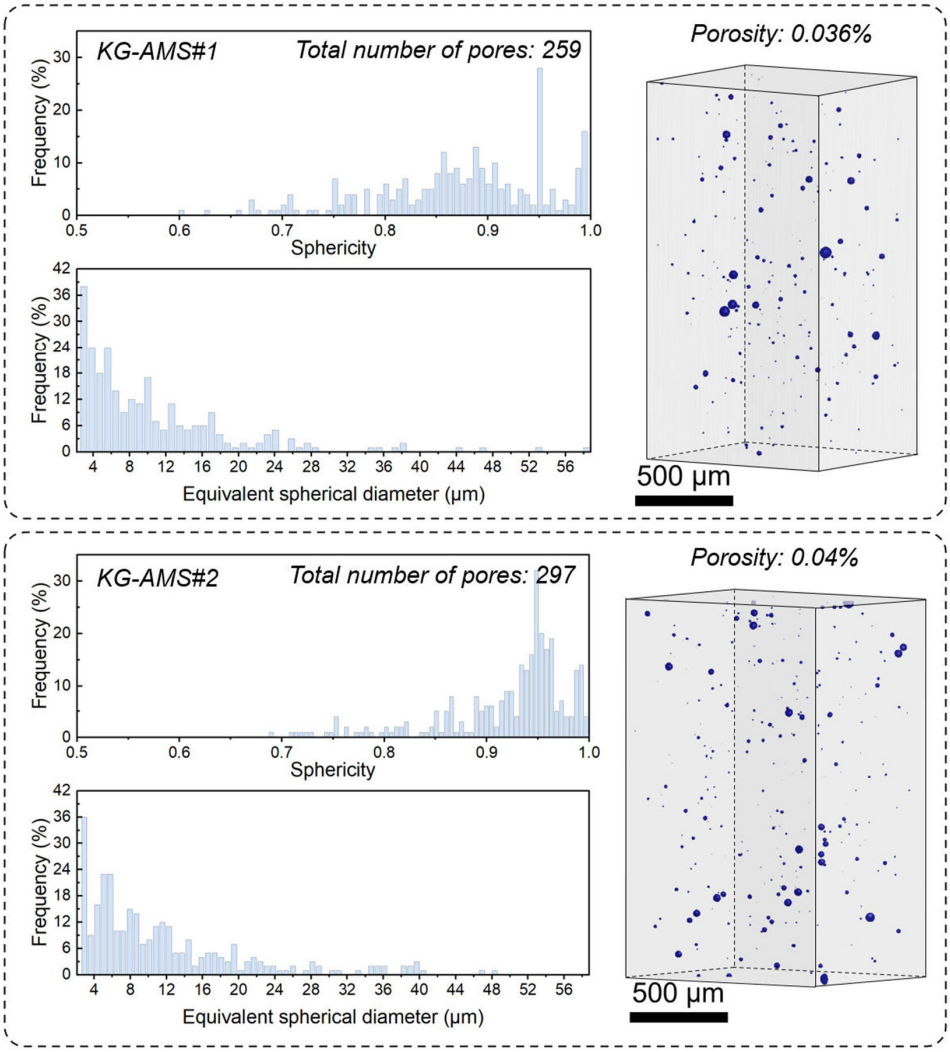

Supplementary Figure 11. High-resolution X-ray CT 3D reconstruction of designed alloy KG-AMS (with a defect area fraction of 0.037%). Two parallel CT samples were examined to check for crack-like features. The volume rendering confirms the absence of crack networks, with only isolated pores detected (sphericity > 0.6), and the measured total porosity values were consistent with the optical-microscopy and UQ-KGAT results described in the text.

Supplementary Note 9: Comparison of defects, hardness, content and size of γ' phase for alloy KG-AMS with all alloys in dataset.

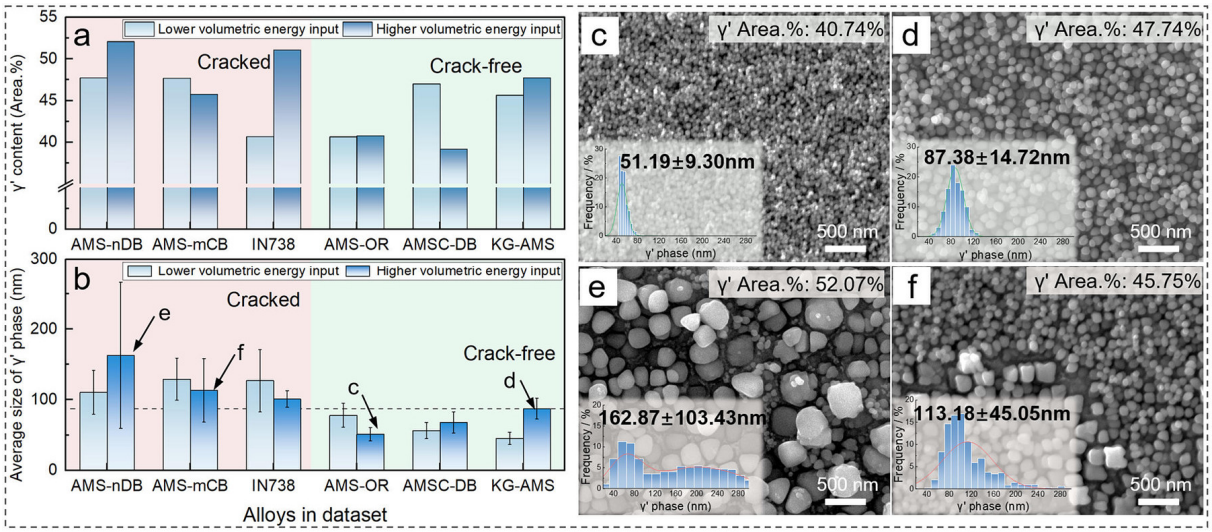

Supplementary Figure 12. Comparison of content and size of γ' phase for alloy KG-AMS with all alloys in dataset under different processing parameters. a γ′ fraction. **b** γ′ size, error bars indicate mean ± SD. **c-f** Representative SEM images of γ′ phase for alloys shown in **b**; the insets show the corresponding γ′ size distributions, with n = 501, 450, 712 and 508 γ′ precipitates for **c**, **d**, **e** and **f**, respectively. Symbols and alloy labels identify the corresponding dataset entries and processing conditions; scale bars are provided in the SEM panels.

Supplementary Figure 12 presents a comparison of the content, size, and morphology of γ′ phase in cracked and crack-free alloys in the dataset, as well as newly designed alloy KG-AMS, at high and low energy densities. It can be observed that cracked alloys typically exhibit a relatively high γ′ phase content, with a large, nearly square γ′ phase size, and a smaller spherical γ′ phase size. In contrast, crack-free alloys have a relatively low γ′ phase content and a smaller spherical γ′ phase size.

To further specify the contributions of hardness, the contributions of the solid solution strengthening effect and the precipitate strengthening effect were calculated as Eq. (S7), and the Hall-Petch effect was considered due to the large grain size in AM-ed alloys[18-21].

$$\sigma_{\mathrm{Y}} = \sigma_{\gamma} + \sigma_{\gamma'} + \sigma_{\mathrm{p}} + \sigma_{\mathrm{Oro}} \tag{S7}$$

The solid solution strengthening effect in AM-ed Ni superalloys is derived from the lattice distortion caused by the entry of refractory metal elements into the FCC matrix and the $L1_2$ precipitate phase. This distortion hinders the movement of dislocations and enhances the mechanical properties of the alloy. The solid solution strengthening effects in the FCC matrix and the $L1_2$ precipitate phase are calculated according to the following equations:

$$\sigma_{\gamma} = \left(1 - f_{\gamma'}\right) \sum_{i} \left(\beta_{\mathrm{i}} \times \sqrt{x_{\mathrm{i}}^{\gamma}}\right) \tag{S8}$$

$$\sigma_{\gamma'} = f_{\gamma'} \sum_i (\beta_i \times \sqrt{x_i^{\gamma'}}) \quad \text{(S9)}$$

where β_i is a strengthening costant for the solution hardening of solute i in γ matrix and γ′ precipitate[18]. $f_{\gamma'}$ is the volume fraction of γ′ phase measured in as-printed samples. x_i^{γ} is the mole fraction of solute i in γ matrix and $x_i^{\gamma'}$ is the mole fraction of solute i in γ′ precipitate, which are calculated using Thermo-Calc software and TCNI12 database.

When the volume fraction of $L1_2$ precipitate was >20%, antiphase boundary (APB) strongly affected the precipitation strengthening. The APB energy can be determined by the linear superposition of the influnece of a single element, and is calculated as follows:[22]

$$\Delta E_{APB} = E_{APB}^0 + \sum_i^n (k_i x_i) \quad \text{(S10)}$$

where k_i is the correlation coefficient for change in APB energy, n is the number of solute elements in γ′ precipitate, x_i is the concentration in at.% of solute i in γ′ precipitate, and E_{APB}^0 is the APB energy for Ni_3Al (195 mJ m^{-2}) measured using TEM by Kruml et al[23].

$$\sigma_p = M\Delta\tau_p \quad \text{(S11)}$$

$$\Delta\tau_p = \frac{\Delta E_{APB} l}{2b(\Lambda + 2\bar{r})} \quad \text{(S12)}$$

$$l = 2(\bar{r}^2 - (\bar{r} - r_{max})^2)^{\frac{1}{2}} \quad \text{(S13)}$$

$$r_{max} = \frac{Gb^2}{2\Delta E_{APB}} \quad \text{(S14)}$$

$$\Lambda = \max\left(\sqrt{\frac{Gb^2\bar{r}}{2\Delta E_{APB}}}\sqrt{\frac{2\pi}{3f_{\gamma'}}}, \sqrt{\frac{2\pi}{3f_{\gamma'}}}\bar{r} - 1\right) \quad \text{(S15)}$$

where M is the Taylor orientation factor and is set to 2.17, G is the shear modulus of the γ′ precipitate, $\bar{r}$ is the mean radius of the γ′ precipitate, b is Burgers vector of the leading a/2<110> dislocation cutting through the precipitates and is equal to 0.257 nm, l is the length of the leading dislocation cutting through the precipitates, r_{max} is the critical precipitate radius at the tradition between weak and strong pair coupling and Λ is an effective distance between the precipitate.

Assuming that the stress required for the dislocation to bypass the $L1_2$ precipitates is less than the stress required for the dislocation to cut the precipitate, the Orowan bypass mechanism also works, and its critical stress is expressed as follows:

$$\sigma_{Oro} = M\frac{3G}{2\sqrt{\frac{2\pi}{3f_{\gamma'}}}\bar{r}} \quad \text{(S16)}$$

According to Eqs. (S7)–(S16), the total strengthening contribution of the designed alloy with a higher energy density was calculated as approximately 521.4 MPa, with the contribution of solid solution strengthening being 191.5 MPa and the contribution of precipitation strengthening being 329.9 MPa. The total strength of the lower energy density was calculated as approximately 612.3 MPa, with the contribution of solid solution strengthening being 192.4 MPa and the contribution of precipitation strengthening being 419.9 MPa. As detailed in Supplementary Table 5, the designed alloy KG-AMS has a higher level of solid solution strengthening and precipitation strengthening, compared to the printable alloys in dataset, such AMS-OR and AMSC-DB. The hard-to-print alloys tend to have higher γ′ phase content, resulting in increased hardness levels.

Supplementary Table 5. The calculated results of strengthening contributions.

Alloys	σ_{γ}	$\sigma_{\gamma'}$	σ_{p}	σ_{Oro}	σ_{Y}
AMS-mCB with higher volumetric energy	158.0	121.1	311.5	65.8	656.4
AMS-mCB with lower volumetric energy	152.4	126.2	296.2	86.0	660.8
IN738 with higher volumetric energy	145.3	133.7	407.9	-	686.9
IN738 with lower volumetric energy	176.2	106.4	331.6	60.8	675
AMS-nDB with higher volumetric energy	102.8	93.1	232.8	99.5	528.2
AMS-nDB with lower volumetric energy	112.1	85.3	281.9	-	479.3
AMSC-DB with higher volumetric energy	120.4	63.5	338.9	-	522.8
AMSC-DB with lower volumetric energy	104.9	76.2	381.9	-	563
AMS-OR with higher volumetric energy	114.7	67.0	373.2	-	554.9
AMS-OR with lower volumetric energy	114.9	66.9	318.4	-	500.2
KG-AMS with higher volumetric energy	110.8	80.7	329.9	-	521.4
KG-AMS with lower volumetric energy	115.3	77.1	419.9	-	612.3

Supplementary Note 10: Pearson coefficient correlation (PCC) and Integrated gradients (IGs).

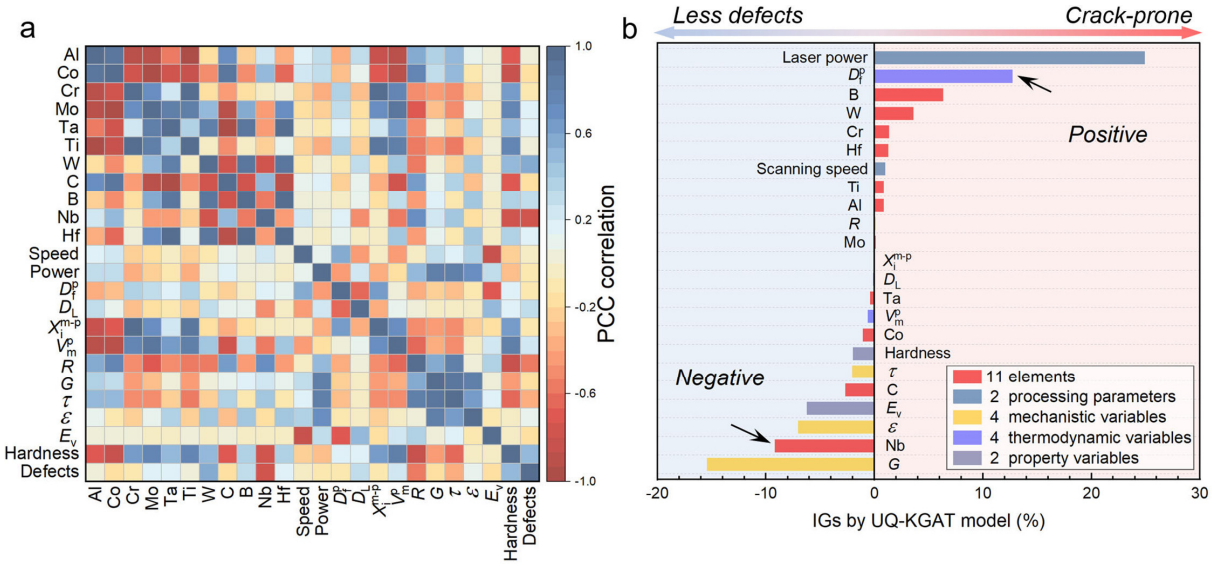

Supplementary Figure 13. Results of feature analysis. a Pearson correlation coefficient (PCC) matrix for all input and output features; the color bar indicates correlation from −1 to 1.; **b** Integrated Gradients (IGs) values from the UQ-KGAT model; positive values indicate features that increase the predicted defect level, whereas negative values indicate features associated with fewer defects. Bar colors denote feature categories: elements, processing parameters, mechanistic variables, thermodynamic variables and property variables.

The correlation between multi-level data features of Ni-based superalloys was analyzed using the Pearson correlation coefficient (PCC). The Pearson coefficient values range from −1 to 1, with values closer to 1 indicating a stronger linear correlation between two features, and values close to 0 indicating a weak linear correlation. As shown in Supplementary Fig. 13a, the absolute value of the Pearson coefficient between any two features is less than 1, indicating that all features can be considered independent variables. Additionally, the absolute value of the Pearson coefficient of each feature relative to the output feature, defect level, is greater than 0, indicating that each feature contributes to the prediction of defect levels.

Notably, Nb, the γ′-phase forming element, exhibits the highest Pearson correlation with defect levels, ranking first among all input features. Key thermodynamic parameters strongly tied to composition—such as the effective diffusion coefficient D_{L}, and the molar volume of the γ′ phase, $V_{\mathrm{m}}^{\mathrm{p}}$—also show prominent correlations, underscoring their close link to defect formation. Furthermore, physical-metallurgical variables directly governed by processing conditions, including solidification growth rate (R), cooling rate (τ), and temperature gradient (G), all display high absolute Pearson coefficients. This reinforces the critical role of additive manufacturing (AM) metallurgical characteristics in defect generation.

To gain a deeper understanding of the UQ-KGAT model's dependence on various features, the Integrated

Gradients (IGs) method was employed to interpret the model's behavior. Integrated Gradients is a sensitivity analysis technique commonly used for interpreting deep learning models. It quantifies the contribution of input features to model predictions. The influence of each feature on the model's output was estimated by computing the integral of gradients along a straight path from a baseline input to the actual input. The core idea is to decompose changes in the input space into infinitesimal steps, accumulating the gradients at each step to derive an overall feature attribution value. The Integrated Gradients are computed as follows[24]:

$$\mathrm{IntergratedGrads}_{\mathrm{i}}(x) ::= (x_{\mathrm{i}} - x'_{\mathrm{i}}) \times \int_{\alpha=0}^{1} \frac{\partial F\left(x' + \alpha(x - x')\right)}{\partial x_{\mathrm{i}}} d\alpha \tag{S17}$$

where, x_{i} represents the actual input feature, x'_{i} denotes the baseline input feature, F is the model's prediction function, and α is the path parameter from the baseline to the input. In the implementation, the Integrated Gradients method was customized and optimized based on the characteristics of the UQ-KGAT model and the specific dataset used. The baseline was set to the minimum value of each feature in the dataset to ensure that the integration path spans the entire range of feature values. This approach helps to more accurately assess the impact of features on the model's output within the actual range of variation.

After computing the attribution value for each sample, we normalized these values such that the sum of the absolute attributions across all features equals 1. This normalization facilitates comparison across different features and emphasizes their relative importance. Positive and negative attribution values reflect the direction of the feature's influence on the model output: Positive attribution values indicate that an increase in the feature leads to an increase in the model's prediction, while negative attribution values suggest that an increase in the feature results in a decrease in the model's prediction.

The results from integrated gradients (IGs) are presented in Supplementary Fig. 13b, offering additional insight into directional relationships. Here, AM process parameters such as laser power show a positive IG with defect formation, whereas the temperature gradient (G) exhibits a negative correlation—again highlighting the strong influence of metallurgical dynamics. Nb displays a negative correlation with defect levels. Among thermodynamic variables, the driving force for γ′ precipitation $D_{\mathrm{f}}^{\mathrm{p}}$ correlates positively with defects, while the γ′ molar volume $V_{\mathrm{m}}^{\mathrm{p}}$ shows a negative trend. These patterns further elucidate the complex interplay between composition and phase structure in determining crack susceptibility in AM alloys.

It is also worth noting that, although laser power holds the highest feature importance in the IG analysis (Supplementary Fig. 13b), its Pearson correlation coefficient is notably low (PCC = –0.086; Supplementary Fig. 13a), indicating a highly nonlinear and process-dependent relationship. In practice, laser power must be finely balanced with other parameters to mitigate defects, adding substantial complexity to process optimization. In contrast, tailoring alloy composition presents a more robust pathway to defect-free printing, as it avoids such intricate processing interdependencies. While individual elemental effects may appear modest compared to laser power, their combined influence is highly significant. Thus, a composition-led strategy offers a more practical and scalable route to reliable AM fabrication.

Supplementary Note 11: Analytical statement on the hot crack susceptibility of the newly designed alloy KG-AMS.

The equilibrium phase composition and the Scheil-Gulliver curve were further determined using the Thermo-Calc software and the TCNI12 database, as shown in Supplementary Fig. 14. The results revealed that the designed alloy KG-AMS contains minimal boride and a significant concentration of primary carbide NbC under equilibrium state. During non-equilibrium solidification, only the γ matrix and primary carbide NbC precipitate. Notably, the presence of NbC enhances the printability, since the phase boundaries between the primary NbC and γ-matrix can act as the trapping sites for boron atoms, thereby helps to suppress the formation of detrimental borides and the emergence of segregation-induced hot cracks[17]. Additionally, a narrow solidification range of approximately 95 K suggests that the alloy demonstrates low susceptibility to hot cracking. Based on these findings, it is reasonable to conclude that the newly designed alloy KG-AMS exhibits superior solidification characteristics, effectively preventing hot cracking during the AM processing.

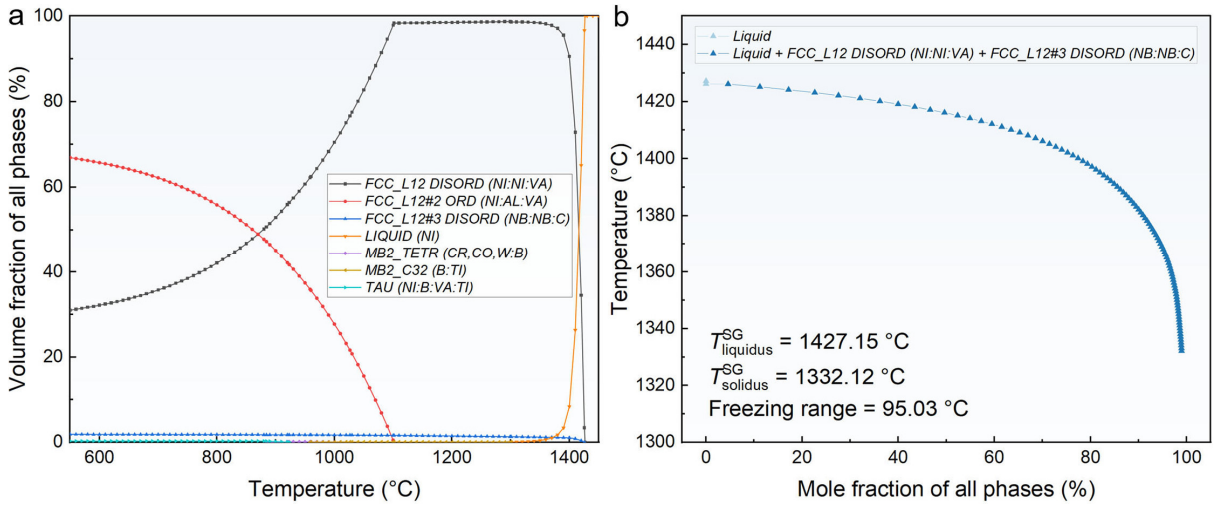

Supplementary Figure 14. Thermo-Calc analysis of KG-AMS. a Calculated phase configuration of KG-AMS alloy. **b** Scheil-Gulliver solidification curve.

Supplementary Note 12: The spatial distribution of the γ′ phase in AM-ed alloy samples and the TEM observations of γ/γ′ phase in the designed alloy KG-AMS.

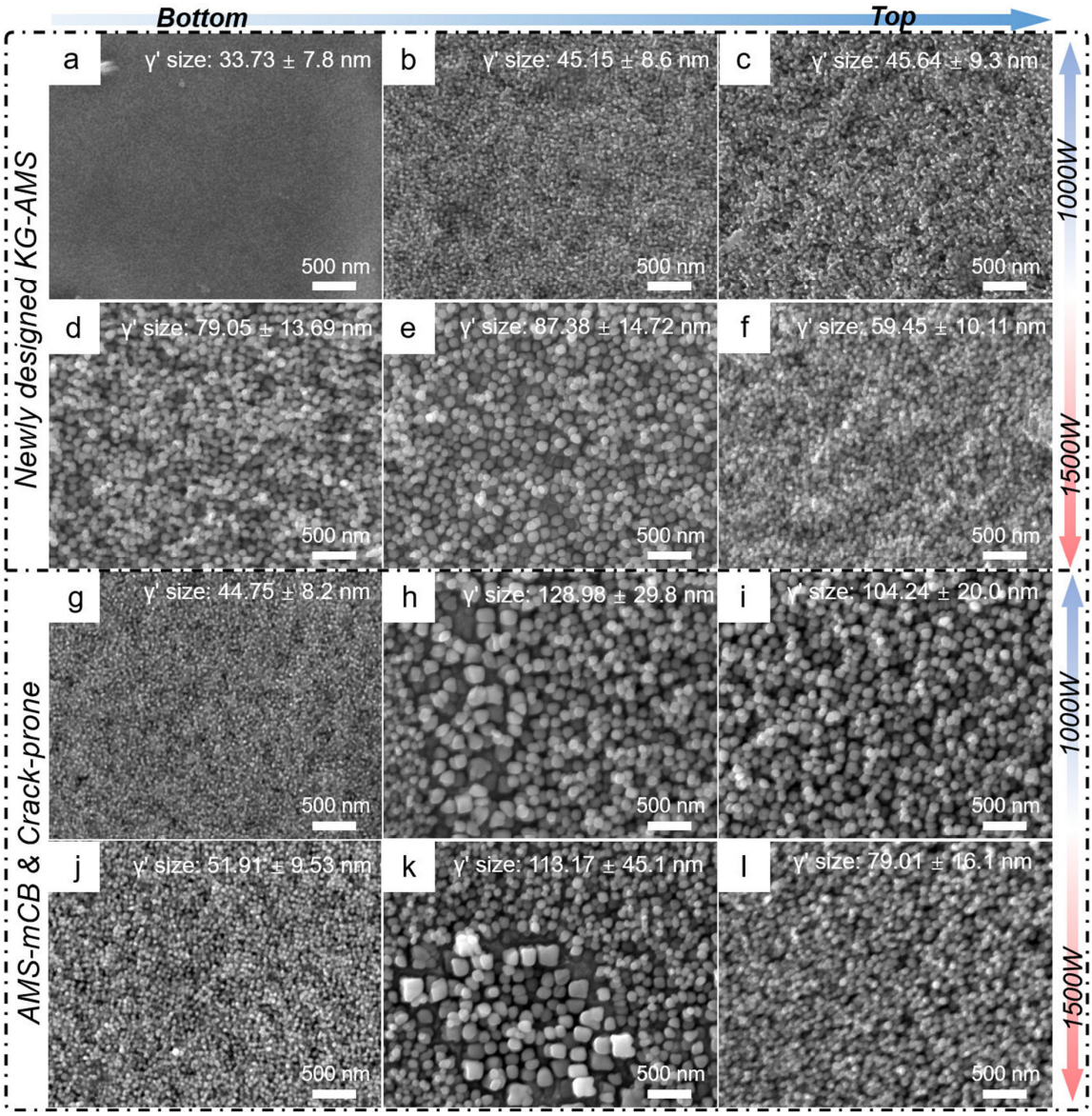

Supplementary Figure 15. Spatial distribution of γ′ phase in KG-AMS alloy and AMS-mCB alloy under different processing parameters. a-c γ′ phase in KG-AMS alloy processed at 1000 W and 10 mm s^{-1}. **d-f** γ′ phase in KG-AMS processed at 1500 W and 10 mm s^{-1}. **g-i** γ′ phase in AMS-mCB processed at 1000 W and 10 mm s^{-1}. **j-l** γ′ phase in AMS-mCB processed at 1500 W and 10 mm s^{-1}.

Supplementary Figure 15 illustrates the spatial distribution of the γ′ phase in the designed alloy KG-AMS and the cracked alloy AMS-mCB under various laser processing conditions. It is evident that alloy KG-AMS consistently exhibits small spherical γ′ phases, whether low energy density (see Supplementary Fig. 15a-c) or high energy density (see Supplementary Fig. 15d-f) processing parameters were applied, suggesting that the γ′ phase in alloy KG-AMS features slow precipitation and coarsening kinetics, low process susceptibility, and excellent thermal stability. In contrast, the γ′ phase in cracked alloy AMS-mCB exhibits significant spatial

variability under laser processing (see Supplementary Fig. 15g-l), particularly noticeable in the central region where larger near-square γ′ phases coexist with smaller spherical γ′ phases, while the lower region predominantly shows very small spherical γ′ phases. This result highlights the cracked alloy AMS-mCB's high susceptibility to processing conditions and extreme susceptibility to thermal history.

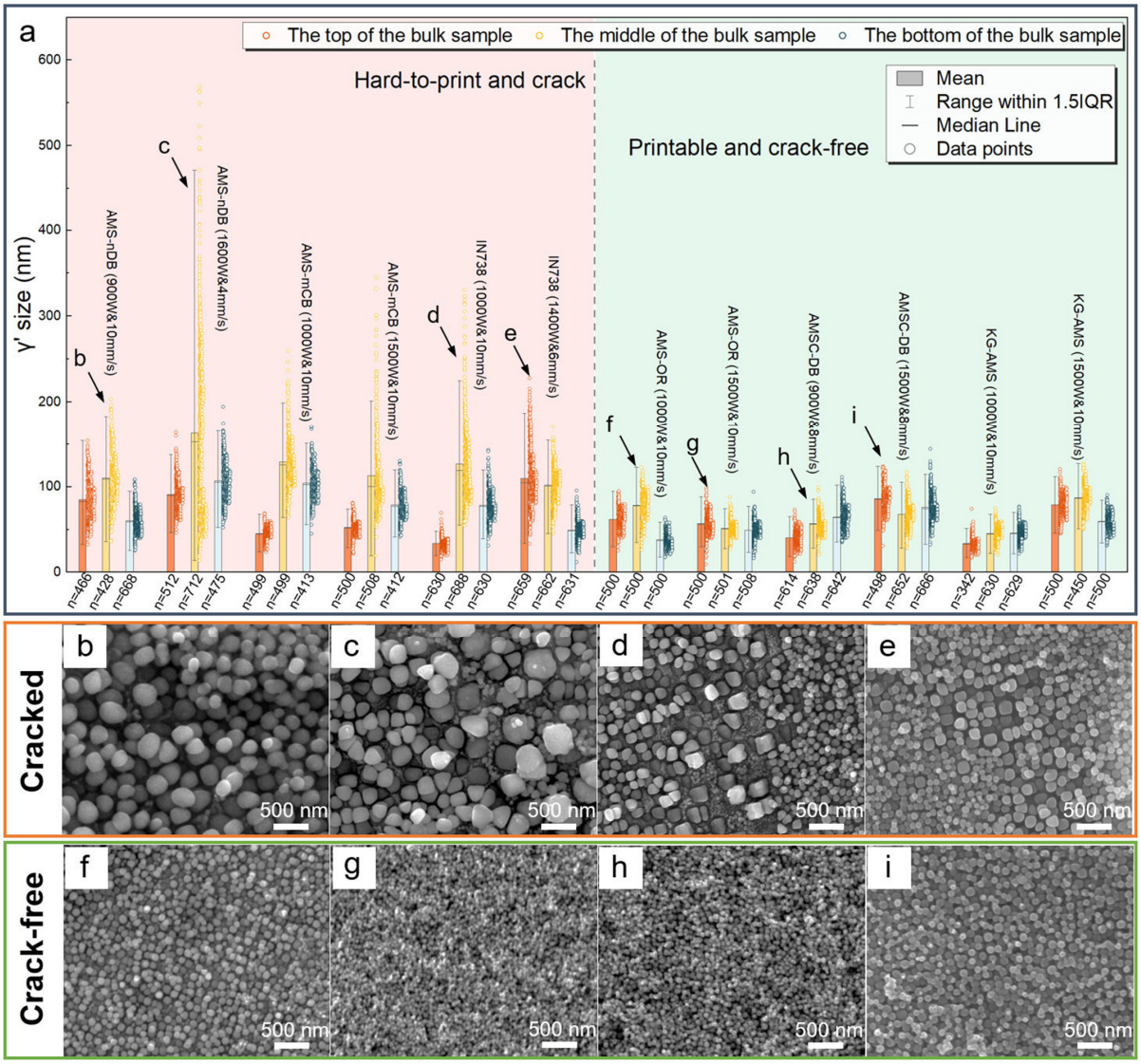

Supplementary Figure 16. Spatial distribution of γ′ phase across cracked and crack-free alloys. a Global overview for all alloys in dataset and the designed alloy KG-AMS. **b**,**c** Cracked alloy AMS-nDB prepared at 900 W/10 mm s^{-1} and 1600 W/4 mm s^{-1}, respectively. **d,e** Cracked alloy IN738 prepared at 1000 W/10 mm s^{-1} and 1400 W/6 mm s^{-1}, respectively. **f,g** Crack-free alloy AMS-OR prepared at 1000 W/10 mm s^{-1} and 1500 W/10 mm s^{-1}, respectively. **h,i** Crack-free alloy AMSC-DB prepared at 900 W/8 mm s^{-1} and 1500 W/8 mm s^{-1}, respectively. Scale bars and region labels are shown in the panels. No inferential statistical tests are shown. Each micrograph is a representative observation for the labelled alloy/condition; no error bars are shown.

Supplementary Figure 16 illustrates a comparison of the spatial distribution of γ′ phases in cracked alloys

and crack-free alloys under various laser processing conditions within the dataset. It is evident that compared to crack-free alloys, γ′ phases in cracked alloys exhibit larger size and significant spatial variation. This observation underscores that γ′ phases in cracked alloys experience accelerated precipitation and coarsening kinetics and are highly sensitive to processing conditions and thermal cycling history.

The complex metallurgical conditions inherent in additive manufacturing involve severe thermal cycling. Layered printing processes induce repeated cycles of dissolution, precipitation, and coarsening of γ′ phases, leading to accumulated phase transformation stresses. Non-uniform rapid precipitation and coarsening of γ′ phases at different positions exacerbate these effects, contributing to crack formation. In cracked alloys, rapid precipitation and growth of γ′ phases result in substantial lattice mismatch stresses. Additionally, uneven precipitation and coarsening of γ′ phases across different spatial positions generate varying stresses at different heights, culminating in elevated residual tensile stresses in the lower sections of cracked alloys[25,26].

As depicted in Supplementary Fig. 17a, the segregation behavior of Nb element during isothermal precipitation for an hour at 1000 °C was simulated using the Thermo-Calc software and its precipitation module. Supplementary Figure 17b presents a comparison of Nb content in γ’ phase across various alloys when the precipitate of γ’ phase reaches a steady-state during the isothermal process. The results demonstrate that, compared to most existing commercial alloys and cracked alloys in the dataset, the crack-free alloys in the dataset, including the designed alloy KG-AMS, printable ADB-900AM alloy, generally exhibit significant partition of Nb in γ’ phase. The finding further confirms that Nb plays a crucial role in influencing the printability of Ni superalloys.

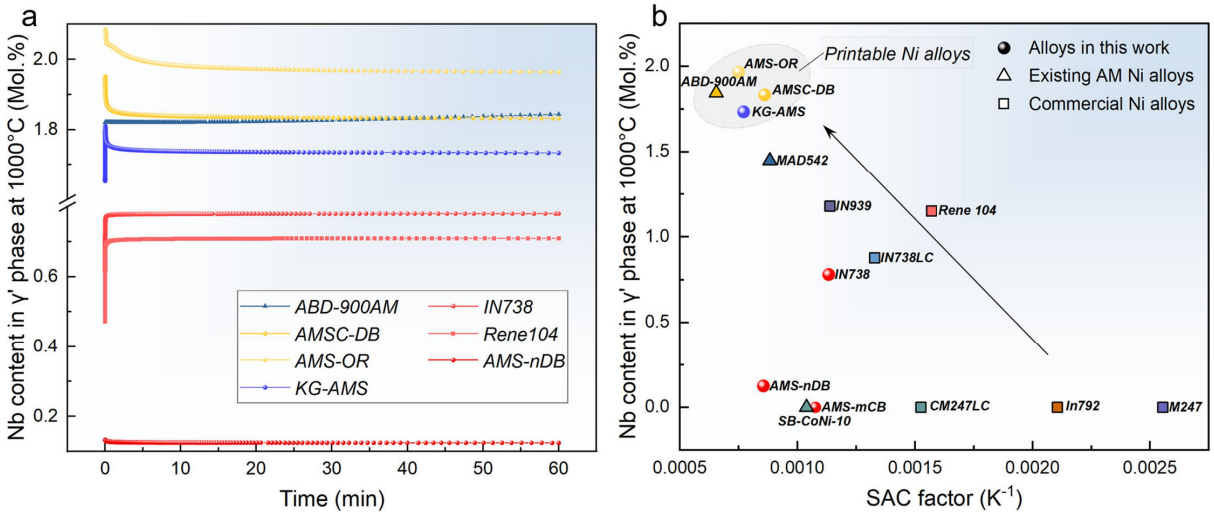

Supplementary Figure 17. Segregation behavior of Nb. a Simulated Nb segregation during isothermal precipitation at 1000 °C for 1 h using Thermo-Calc. **b** Comparison of Nb content in the γ′ phase for existing additively manufactured Ni alloys and commercial Ni alloys when the γ′ precipitate reaches steady state. Symbols, alloy groups and colors are defined in the panel. These data are simulations and literature/dataset comparisons; no inferential statistical tests are shown.

The experimental observations in Supplementary Fig. 18a illustrate the elemental distribution of the γ matrix phase and the γ′ precipitation phase in the designed alloy KG-AMS, showing an enrichment of Nb and Ta elements in the γ′ phase. Supplementary Figure 18b and c present selected area electron diffraction and high-resolution results, respectively, revealing the lattice parameters of the γ matrix phase and the γ′ precipitate phase. The lattice mismatch value between the γ matrix phase and the γ′ precipitate phase is -0.081%, confirming that the designed alloy KG-AMS has a low level of lattice mismatch, resulting in the sluggish precipitation and coarsening behavior of the γ′ phase, thereby leading to the low residual stress and reduced cracking susceptibility.

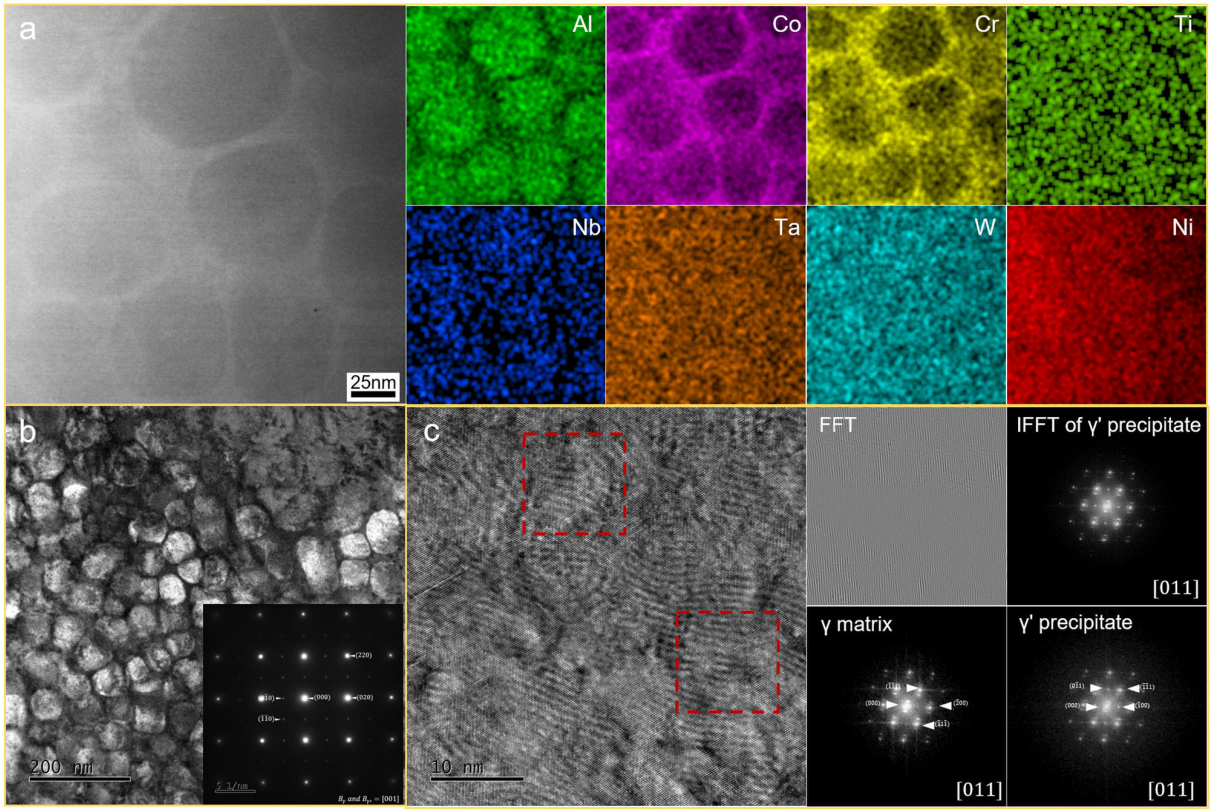

Supplementary Figure 18. TEM observations of γ/γ′ phase in KG-AMS alloy. a STEM-HAADF image and corresponding elemental maps of Al, Co, Cr, Ti, Nb, Ta, W and Ni. **b** Dark field micrograph with selected-area electron diffraction pattern. **c** High-resolution TEM image with FFT and IFFT analysis of the γ matrix and γ′ phase showing the coherent interface. Element-map colors correspond to the element labels in the panels, and scale bars are shown in the images. No inferential statistical tests are shown. Each microscopy panel is a representative observation; no error bars are shown.

Supplementary Figure 19 shows neutron diffraction results for the upper part and the lower part of the bulk in AMS-mCB alloy, which gives the specific lattice parameters and lattice misfit of γ/γ' phase.

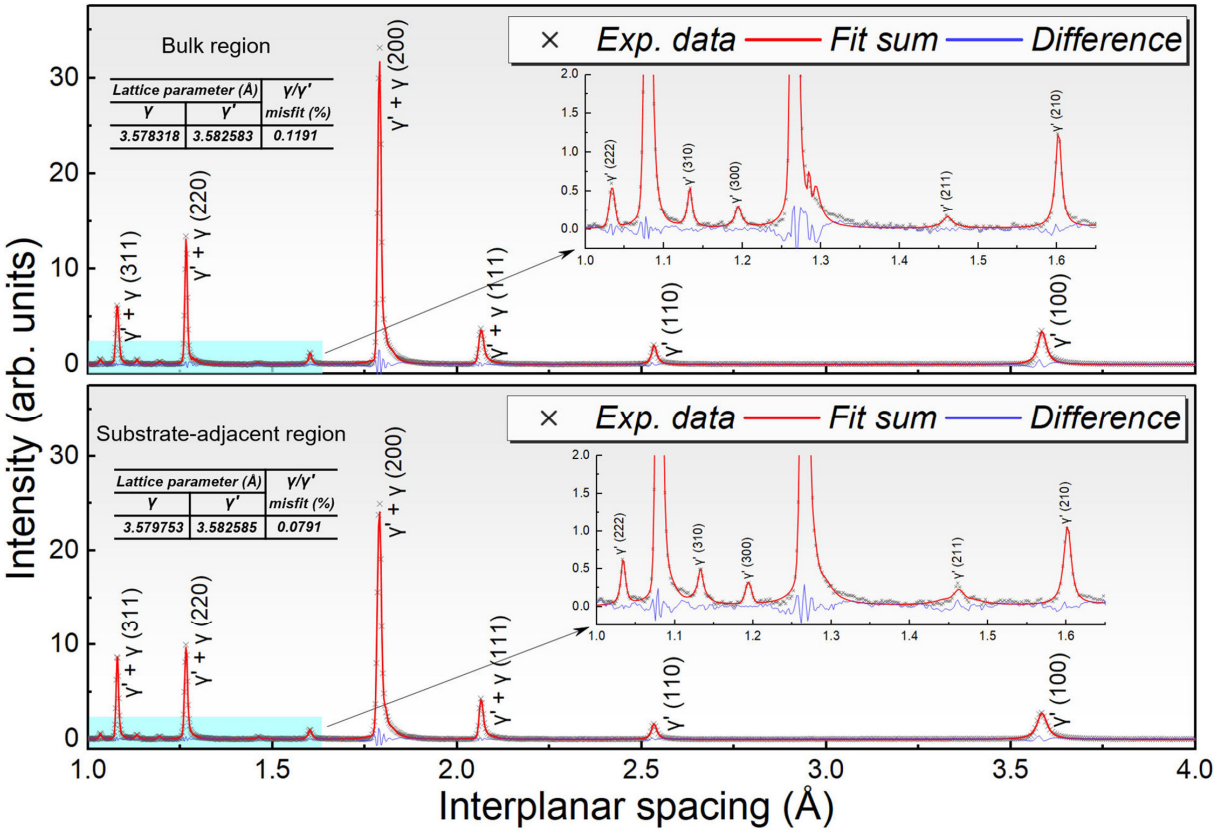

Supplementary Figure 19. Neutron diffraction analysis of γ/γ′ lattice parameters in the upper bulk region and substrate-adjacent region of AMS-mCB. Black crosses denote experimental data, red curves denote the fitted peak sum and blue curves denote the fit residual/difference. Insets magnify the highlighted low-intensity peak regions, and embedded tables report the fitted γ and γ′ lattice parameters and the corresponding γ/γ′ misfit.

Supplementary Note 13: The mechanical properties of the designed alloy KG-AMS.

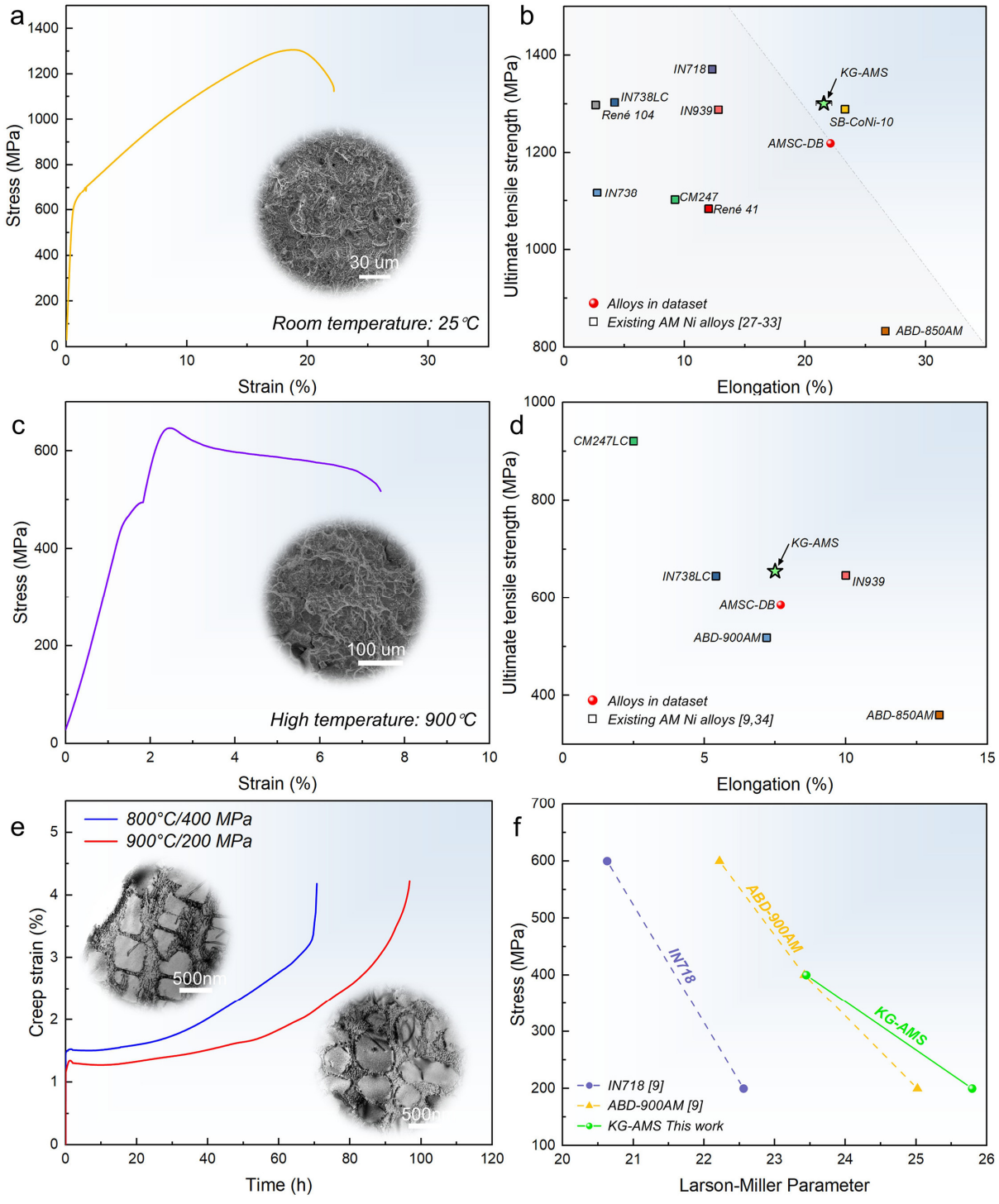

Supplementary Figure 20. Mechanical properties of newly designed additive manufacturable Ni superalloy KG-AMS. a Room-temperature tensile response of KG-AMS. **b** Room-temperature tensile-property comparison with other additively manufactured alloys[27-33]. **c** Tensile response of KG-AMS at 900 °C. **d** High-temperature tensile-property comparison with other additively manufactured alloys[9,34]. **e** Creep property of heat-treated KG-AMS tested at 800 °C/400 MPa and 900 °C/200 MPa respectively. **f** Comparison

of creep property for KG-AMS with other additive manufacturable alloys after heat treatment[9].

The tensile properties and creep performance of the KG-AMS alloy were rigorously assessed, as shown in Supplementary Fig. 20. The heat treatment strategy comprised the following steps: standard stress relieving at 1065 ℃ for 1.5 h with a cooling rate of 6 ℃ min^{-1} to 500 ℃ to reduce the residual stress[30], and then followed by 1300 °C/2 h, AC (solution) + 900 °C/24 h, AC (aging). After heat treatment, as shown in Supplementary Fig. 20a-d, the room-temperature tensile strength of alloy KG-AMS reaches 1307 MPa with an elongation of 22.2%, representing an excellent strength-ductility combination that surpasses most reported additively manufactured Ni-based superalloys and is comparable to the high-performance alloy SB-Ni-10. Notably, it also outperforms the crack-free alloy AMSC-DB from the input database (tensile strength: 1219 MPa, elongation: 22.1%). Furthermore, we have performed additional high-temperature tensile tests at 900 °C, showing that KG-AMS achieves a tensile strength of 655 MPa and an elongation of 7.5%. This performance is superior to that of other printable alloys such as AMSC-DB, ABD-900AM, and ABD-850AM, while matching the strength of the hard-to-print alloys IN738LC and IN939.

Supplementary Figure 20e presents the creep fracture curves for the heat-treated alloy KG-AMS subjected to conditions of 900 ℃/200 MPa and 800 ℃/400 MPa. The curves reveal that the creep rupture life of the alloy diminishes with an increase in test stress, registering 97.8 hours and 70.7 hours under the respective conditions. Furthermore, the creep rupture process can be segmented into three distinct stages: the primary, secondary, and tertiary stages, with the secondary stage constituting a significant portion of the entire creep life. This stage is crucial as it exemplifies the alloy's creep and fracture characteristics, representing 81% and 85% of the total duration under the conditions of 900 ℃/200MPa and 800 ℃/400MPa, respectively.

To demonstrate the superior creep resistance of alloy KG-AMS, a Larson-Miller Parameter (LMP) diagram (Supplementary Fig. 20f) was constructed, which facilitates a comparison of alloy KG-AMS's creep resistance with that of the existing printable Ni superalloys such as IN718 and ABD-900AM under various conditions. The LMP is defined as follows[9]:

$$\mathrm{LMP} = T \times \frac{20 + \log t_{\mathrm{r}}}{1000} \tag{S18}$$

where T is the absolute temperature, in Kelvin, and t_r is the time of rupture. It is worth noting that the highly machinable alloy IN718 shows the worst creep properties, especially at high temperature, which is due to its intermetallic phase instability and low oxidation resistance. Compared to the newly designed additive manufacturable ABD-900AM alloy, the KG-AMS alloy features a higher γ′ content of approximately 45%, alongside a well-optimized heat treatment process and a stable microstructure. Consequently, it exhibits superior creep resistance at high temperatures and low stress levels.

To further evaluate the overall suitability of designed KG-AMS alloy for high-temperature applications, a direct comparison of key properties, including yield strength, elongation between our alloy and existing AM-ed Ni-based superalloys is provided in Supplementary Fig. 21, where the core design objective of defect area

fraction is presented as well. Although its yield strength at room temperature is modest (comparable to that of the highly printable alloy SB-CoNi-10, see Supplementary Fig. 21a), the critical advantage lies in its minimal strength loss at high temperatures. The designed alloy exhibits the smallest strength loss among the compared materials when tested at elevated temperature, decreasing from 627 MPa at 25 °C to 482 MPa at 900 °C (see Supplementary Fig. 21b). This minimal attenuation, combined with the lowest defect area fraction achieved, demonstrates the alloy's potential for reliable performance under thermal load.

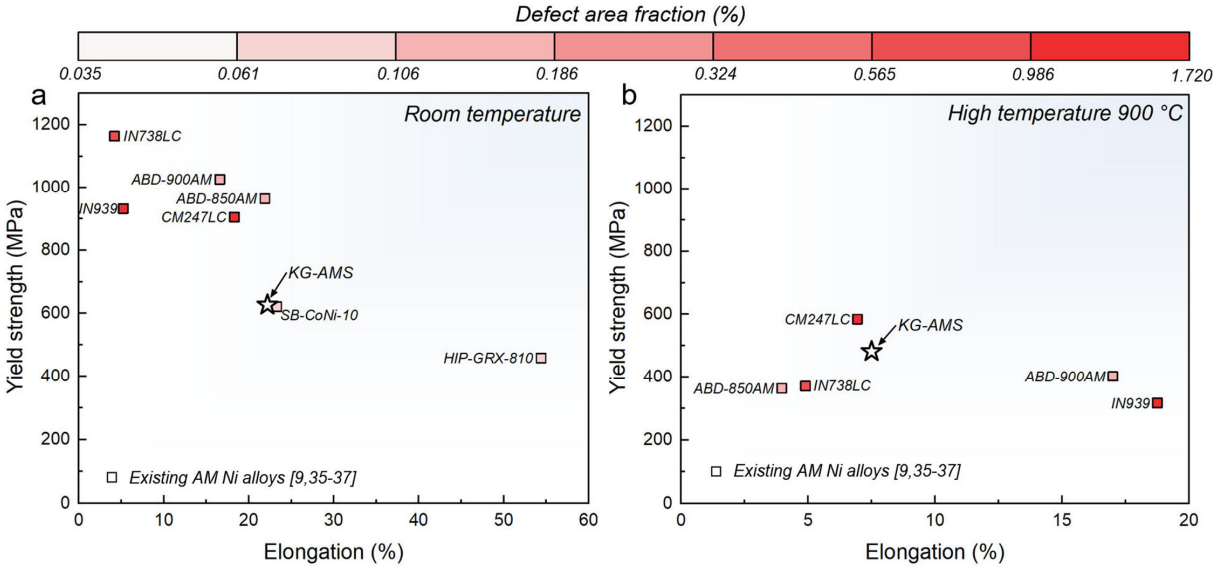

Supplementary Figure 21. Comparison of yield strength and elongation for KG-AMS with other AM-ed Ni superalloys[9,35-37]. **a** Room-temperature comparison. **b** High-temperature comparison at 900 °C. Symbols identify the compared alloys and literature sources as labelled in the panels.

Supplementary Note 14: Design details and Analysis of the designed alloy KG-AMAA.

To further validate the universality of the graph attention network model, which is based on a physical metallurgy knowledge graph and uncertainty quantification, we conducted the design of composition and process and computational analysis for additive manufacturing of aluminum alloys. Specifically, we established a dataset of 163 Al alloy samples prepared using Laser Powder Bed Fusion (L-PBF) technology, grounded in a comprehensive literature review[38-49]. The Al alloy dataset encompasses a broad spectrum of alloy systems, including Al12Si, AlSi10Mg, AA2024, AA6061, AA7075+Zr, AlMgZnSi, and Scalmalloy® (as detailed in Supplementary Table 6), thereby ensuring compositional diversity. As further shown in Supplementary Table 7, the dataset includes 15 input features that encompass both material properties and process parameters. The material properties cover 9 elemental compositional features (e.g., Si, Fe, Cu, Mg, Sc, Zr, Mn, Zn, Ni), while the processing parameters include laser power, scanning speed, spot size, hatch space, layer thickness, and the platform temperature. Additionally, the material's hardness is also incorporated into the model to fully assess the coupled characteristics of the L-PBF process and material properties.

Supplementary Table 6. The commercial Al alloys and Scalmalloy® (in wt.%) used in the dataset.

Alloys	Si	Fe	Cu	Mg	Sc	Zr	Mn	Zn	Ni	Al
Al12Si	12.2	0.12	0.003	0	0	0	0	0	0	Bal.
AlSi10Mg	9.83	0	0	1.19	0	0	0	0	0	Bal.
AA2024	0.5	0.5	4.9	1.8	0	0	0.9	0	0	Bal.
AA6061	1.2	0.9	0.32	0.77	0	0	0	0	0	Bal.
AA7075-Zr	2.9	0.5	1.47	1.9	0	1	0	5.1	0	Bal.
AlMgZnSi	1.96	0.17	0	5.39	0	0	0.75	3.08	0	Bal.
	0.04	0.15	0	14.6	0.35	0.21	0	0	0	Bal.
	0.14	0.08	0.44	3.4	1.08	0.23	0	0.07	0	Bal.
Scalmalloy®	0.14	0.08	0.44	3.4	1.08	0	0.5	0.23	0	Bal.
	3	0	0	2.2	0.4	0.2	0	6.5	0	Bal.
	0	0	0	2.5	0.4	0.1	0	0	1	Bal.

The model's output, namely the relative density (as measured by Archimedes' principle and calculated relative to theoretical density), serves as a metric to evaluate the printing performance of L-PBF-processed Al alloys[38,43,44,46,48-52]. Moreover, 4 solidification mechanism variables closely related to additive manufacturing—such as temperature gradient, solidification growth rate, cooling rate, and solidification parameters—were introduced based on finite element simulations, as detailed in Supplementary Note 2. Two dimensional thermodynamic variables, including the volume fraction of the α-Al matrix phase and the effective diffusion coefficient, were derived from calculations using Thermo-Calc software and the TCAL6

database. Furthermore, we constructed a knowledge graph based on the hierarchical relationships among different data features and principles of physical metallurgy. The knowledge graph was then used to guide the training of the attention network model. By integrating the uncertainty method, the model quantitatively predicts the relative density of AM-ed Al alloys while also assessing both statistical and model uncertainties.

Supplementary Table 7. Input and output ranges of the parameters in the AM-ed Al alloy dataset.

	Features	Maximum	Minimum	Mean	Standard deviation
Inputs	Silicon (wt.%)	12.2	0	4.04	4.83
	Iron (wt.%)	0.9	0	0.24	0.27
	Copper (wt.%)	4.9	0	1.32	2.07
	Magnesium (wt.%)	14.6	0	2.53	3.30
	Scandium (wt.%)	1.08	0	0.17	0.33
	Zirconium (wt.%)	1	0	0.07	0.18
	Manganese (wt.%)	0.9	0	0.27	0.40
	Zinc (wt.%)	5.1	0	0.28	1.04
	Nickel (wt.%)	1	0	0.12	0.32
	Power (W)	370	100	260.09	79.73
	Speed (mm s^{-1})	3000	98	989.09	635.16
	Spot size (um)	100	70	82.72	10.31
	Hatch space (mm)	0.5	0.04	0.14	0.11
	Layer thickness (um)	60	20	30.93	7.60
	Platform temperature (°C)	500	35	97.31	98.20
	Temperature gradient (K m^{-1})	3.04E+07	5.74E+06	1.78E+07	6.41E+06
	Growth rate (m s^{-1})	0.0563	0.0336	0.0435	0.0048
	Cooling rate (K s^{-1})	1.58E+06	2.23E+05	7.79E+05	3.09E+05
	Solidification parameter (K·s m^{-2})	7.4E+08	1.48E+08	4.11E+08	1.48E+08
	Diffusion coefficient (m^2 s^{-1})	4.53E-14	2.66E-24	1.69E-15	8.54E-15
	Volume Fraction of FCC_A1	0.9728	0.2339	0.8637	0.1293
	Hardness (HV)	160.79	53.94	103.32	24.46
Output	Archimedes' density (%)	99.98	86.51	97.47	2.31

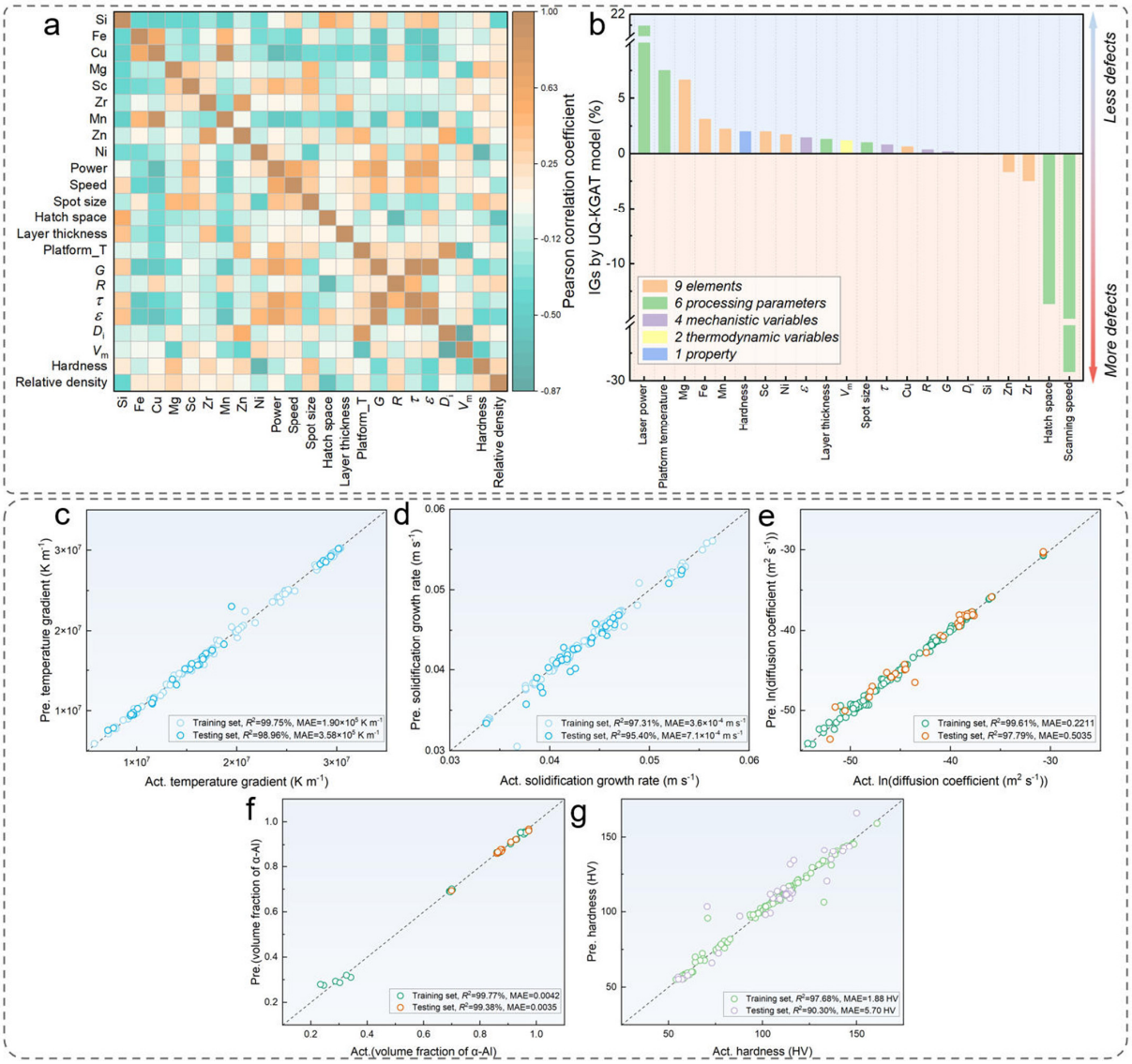

Supplementary Figure 22. Feature analysis and intermediate-variable prediction for the L-PBF Al-alloy dataset. a PCC matrix of all features. **b** IGs value between input features and output from the UQ-KGAT model. **c-g** Prediction of intermediate variables: temperature gradient, solidification growth rate, diffusion coefficient, volume fraction of α-Al phase and hardness. The Al dataset contains n = 163 L-PBF-processed samples; color scales, feature categories and R^2 metrics are defined in the panels.

Supplementary Figure 22a displays the Pearson Correlation Coefficients (PCC) among all features, ranging from -0.9 to 1. Supplementary Figure 22b presents the Integrated Gradients (IG) values derived from the UQ-KGAT model, underscoring the significance of L-PBF metallurgical characteristics on the relative density of Al alloys. Supplementary Figure 22c-g illustrate the high-precision predictive performance of traditional machine learning models on AM metallurgy mechanistic variables, thermodynamic variables, and hardness. The R^2 values for the testing set for all predictions exceed 90%, demonstrating the models' high accuracy.

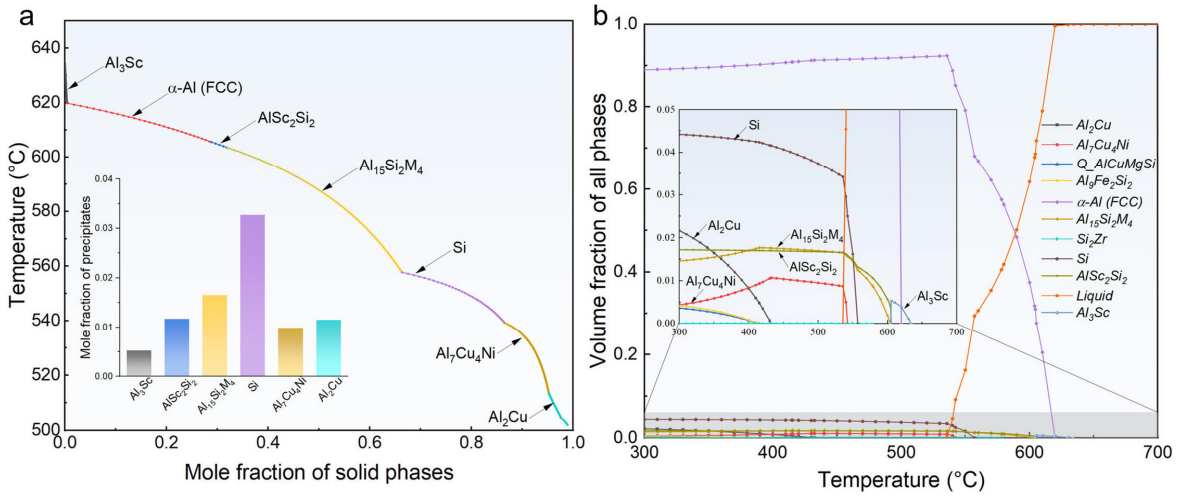

Supplementary Figure 23. Thermo-Calc analysis of KG-AMAA. a Calculated Scheil-Gulliver solidification curve. **b** Calculated phase configuration of KG-AMAA alloy. Phase labels, colors and temperature-dependent quantities are defined in the panels.

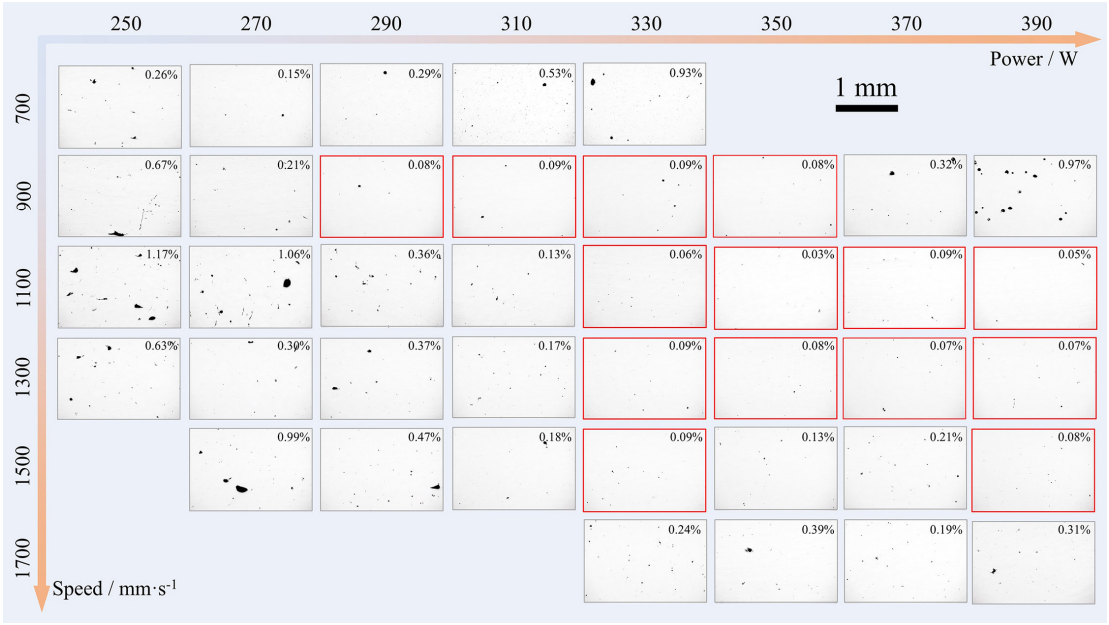

Supplementary Figure 24. Experimental validation of designed Al alloy KG-AMAA using L-PBF technology at different processing parameters. Columns indicate laser power from 250 to 390 W and rows indicate scanning speed from 700 to 1700 mm s^{-1}; hatch spacing, layer thickness and laser spot size were fixed at 0.1 mm, 30 μm and 80 μm, respectively. Percentages in each optical micrograph indicate the measured defect level for that condition. Red frames highlight the low-defect processing window and the scale bar is 1 mm.

The critical freezing range criterion (ΔT) is then employed to assess the hot crack susceptibility of the alloy.

$$\Delta T = |T^{SG}_{f_s=0.97} - T^{SG}_{f_s=0.80}| \quad \text{(S19)}$$

The value of ΔT was calculated as Eq. (S19)[53], to evaluate the hot-cracking susceptibility of L-PBF-processed Al alloys, and is calculated using Scheil-Gulliver model based on Thermo-Calc software and

TCAL6 database.

As shown in Supplementary Fig. 25a, the as-printed KG-AMAA alloy exhibits excellent mechanical properties, with a yield strength (YS) of 287 MPa, ultimate tensile strength (UTS) of 454 MPa, and total elongation of 9.5%. It is crucial to note that the aluminum alloy case is presented primarily to validate the universality of our design framework beyond Ni-based superalloys, focusing on intrinsic strength enhancement. For a fair and focused assessment, the comparison in Supplementary Fig. 25b is strictly limited to as-printed properties and excludes composites, which prevents the conflation of different strengthening mechanisms and allows for a meaningful evaluation of our alloy design strategy under process-agnostic conditions.

Notably, the conventionally designed SLM-ed AlZnMgCuScZr alloy[54] exhibits unprecedented strength–ductility synergy, representing significant engineering value. However, its reported relative density under specific printing conditions is slightly lower than that of the alloy developed here, making its printability a critical topic for further systematic study. So, it should be emphasized that (1) Our primary goal was not to develop an ultra-high-performance alloy for extreme conditions, but to design a high-value alloy with the widest printing window among existing alloys, whose performance suffices for most engineering applications. (2) Even when considering only strength–ductility synergy, our alloy ranks as the second-best performer reported over the past decade (2014–2024). The discovery of this alloy within half a year, accelerated by the AI algorithm presented here, underscores the method's significant value and innovation in materials development. In summary, we developed an alloy that displays among the best printability and the second-highest strength–ductility product so far.

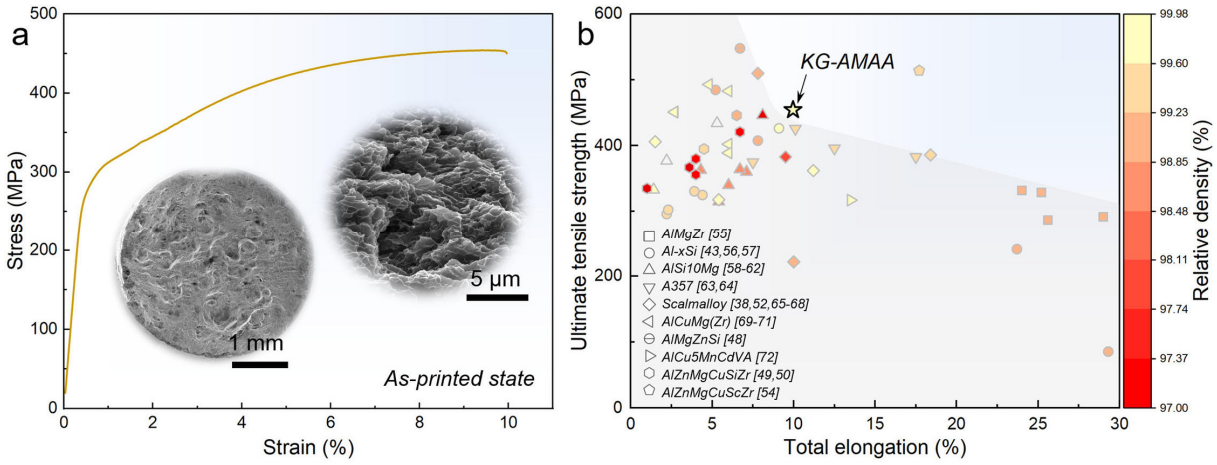

Supplementary Figure 25. Mechanical properties and printability comparison for as-printed KG-AMAA. a Stress-strain curve of designed KG-AMAA alloy at as-printed state. **b** Comparison of printability and tensile properties for as-printed Al alloys fabricated via additive manufacturing (AlMgZr[55], Al-xSi[43,56,57], AlSi10Mg[58-62], A357[63,64], Scalmalloy®[38,52,65-68], AlCuMg(Zr)[69-71], AlMgZnSi[48], AlCu5MnCdVA[72], AlZnMgCuSiZr[49,50], AlZnMgCuScZr[54]), excluding composites and heat-treated conditions.

Supplementary Note 15: Analysis of the novelty of designed alloys KG-AMS and KG-AMAA

To evaluate the novelty of the designed alloys, we performed principal component analysis (PCA). As shown in Supplementary Fig. 26a, the Ni-based alloy KG-AMS lies in a distinct region above the intersection of cast and wrought alloy clusters and is clearly separated from other AM-optimized alloys (e.g., ABD series, MAD542). Similarly, KG-AMAA occupies a unique position in the Al alloy PCA projection (Supplementary Fig. 26b), differing from both conventional and existing AM aluminum alloys. This confirms that our model identifies novel compositional combinations even within a broad known domain.

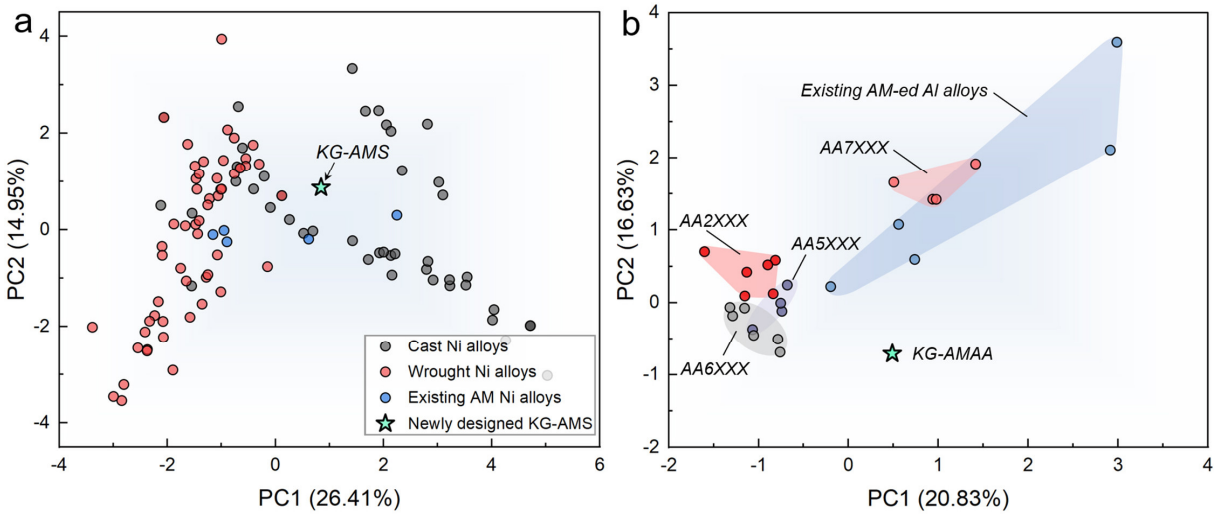

Supplementary Figure 26. Principal component analysis of designed alloys relative to reported composition spaces. a PCA projection of Ni superalloys[1], showing the distinct location of KG-AMS. **b** PCA projection of Al alloys[38,39,42,43,46,48,50-52,73], highlighting the unique composition of KG-AMAA. Axes report principal component scores, and colors/symbols identifying alloy groups are defined in the panels.

To further examine the compositional robustness of designed alloy KG-AMAA, a sensitivity analysis was conducted around its nominal composition. As shown in Supplementary Figure 27, the fluctuation ranges defined for the key elements in KG-AMAA are as follows: Si ±0.5 wt.%, Fe ±0.1 wt.%, Cu ±0.2 wt.%, Mg ±0.05 wt.%, Sc ±0.1 wt.%, Zr ±0.001 wt.%, Mn ±0.05 wt.%, Zn ±0.05 wt.%, and Ni ±0.05 wt.%. Among these, Si, Cu, and Sc are identified as the elements exerting the most pronounced influence on printing performance. Importantly, even under the maximum tested variations in these elements, the relative density remains above 99.96%. Overall, the composition of KG-AMAA displays strong robustness: variations in most elements yield relative densities exceeding 99.98%, a value higher than the maximum relative density observed in the original dataset.

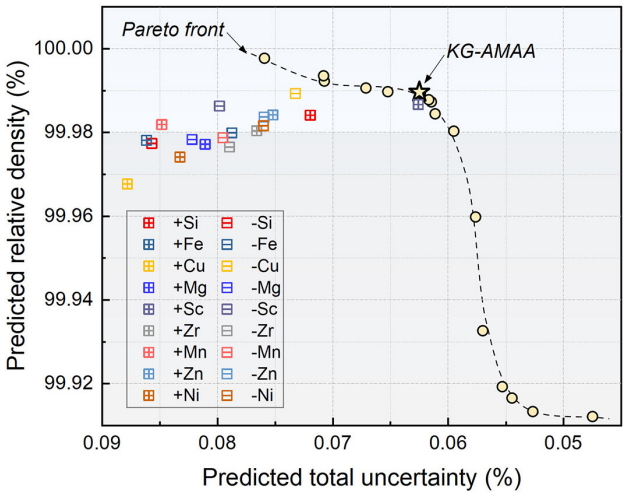

Supplementary Figure 27. Effects of compositional perturbations on predicted relative density and uncertainty for KG-AMAA. The positive and negative deviations of concentrations are indicated by "+" or "–" in the symbols, respectively. The perturbation ranges were Si ±0.5 wt.%, Fe ±0.1 wt.%, Cu ±0.2 wt.%, Mg ±0.05 wt.%, Sc ±0.1 wt.%, Zr ±0.001 wt.%, Mn ±0.05 wt.%, Zn ±0.05 wt.% and Ni ±0.05 wt.%.

Supplementary Note 16: The description of simulation for thermal history during additive manufacturing based on finite element method.

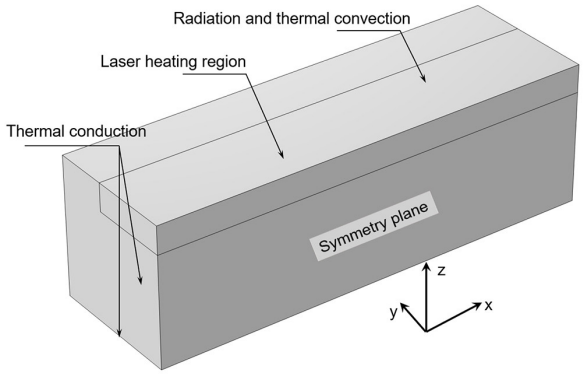

Supplementary Figure 28. Computational domain and boundary conditions for the finite-element simulation of L-DED thermal history. The schematic defines the laser heating region, radiation and thermal-convection boundary on the upper surface, thermal-conduction boundary, symmetry plane and x-y-z coordinate system. The model geometry and assumptions are described in the accompanying Supplementary Note 16.

To better understand the impact of physical metallurgical conditions on the microstructure of Ni-based superalloys, the thermal history and solidification behavior during the Laser Directed Energy Deposition (L-DED) single-track printing process were simulated using the finite element method. Mechanistic variables influencing cracking were calculated based on a transient three-dimensional heat transfer and fluid flow model[2-5]. Several reasonable assumptions are made as follows[74-78]: (1) Liquid metal flow within the molten pool is considered Newtonian, laminar, and incompressible. (2) Vaporization is neglected due to the system's calculated peak temperature being below the material's boiling point. (3) The mushy zone, where temperatures range between the solidus and liquidus, is modeled using a porous medium with isotropic permeability. (4) The influence of shielding gas is disregarded due to its minimal pressure. (5) Powder instantaneously melts upon contact with the deposition surface and is treated as a continuous and uniform phase.

Governing equation

The heat transfer energy equation in all domains is defined as (S20):

$$\rho C_{\mathrm{p}}\left(\frac{\partial T}{\partial t}+\boldsymbol{u}\cdot\nabla T\right)=-\nabla\cdot\boldsymbol{q}+Q \tag{S20}$$

where, ρ is the density, C_{p} is the specific heat capacity, T is the temperature, t is the time, $\boldsymbol{u}$ is the speed, $\boldsymbol{q}$ is the heat flux and given by the Fourier's conduction equation, as shown in Eq.(S22), Q is the heat rate per unit of volume, as defined as Eq.(S24).

$$\boldsymbol{q}=-k\nabla T \tag{S21}$$

where, k is the thermal conductivity.

Velocities of the metal inside the molten pool are regarded as incompressible fluids and can be calculated by solving the following Navier-Stokes equation (S22) and the continuity equation (S23).

$$\rho\left(\boldsymbol{u}_{,\mathrm{t}}+\boldsymbol{u}\cdot\nabla\boldsymbol{u}-g\right)+\nabla\boldsymbol{p}-2\mu\Delta\boldsymbol{u}=0 \tag{S22}$$

$$\nabla\cdot\boldsymbol{u}=0 \tag{S23}$$

where $\boldsymbol{u}$ is the velocity field, $\boldsymbol{p}$ is the pressure field, g is the gravity acceleration vector, ∇ is the gradient operator, Δ is the Laplace operator, ρ and μ are density and dynamic viscosity, respectively.

Initial and boundary conditions

The substrate and cladding are assumed to be initially at the ambient temperature T_0 and pressure P_0, and at a zero initial velocity field. The heat flux at the interface is defined as:

$$Q=\frac{2P\eta_{\mathrm{l}}}{\pi r_{\mathrm{b}}^2}exp(\frac{-2((x-vt)^2+y^2)}{r_{\mathrm{b}}^2})-\hbar_{\mathrm{c}}(T-T_0)-\sigma_{\mathrm{b}}\eta(T^4-T_0^4) \tag{S24}$$

where P is the laser power, η_{l} is the absorption of laser energy, x and y are the distance to the laser, r_b is the effective laser beam radius, v is the scanning speed, $\hbar_{\mathrm{c}}$ is the heat transfer coefficient, σ_{b} is the Stefan-Boltzmann constant, η is the emissivity.

The computational domain and boundary conditions are illustrated in Supplementary Fig. 28. The laser heat source is positioned on the top surface of the cladding. Radiation and convection heat transfer are applied to the upper surface of both the substrate and the cladding layer. Heat conduction within the metal is considered for the surrounding areas and the bottom of the substrate. Additionally, a fixed constraint is applied at the bottom. The computational domain includes a substrate with the dimensions of 5×10×5mm^3 and a single track with the length of 10 mm. The maximum time step is 1×10^{-2} s. Simulations were performed on a ROG computing station (64×2.30 GHz, 128 GB).

Supplementary Table 8. Processing parameters used in this study.

Parameters	Value
Laser power, W	600-1600
Scanning speed, mm s^{-1}	4-14
Absorptivity	0.6
Powder feed rate, g min^{-1}	7
Layer thickness, mm	0.7
Laser beam radius, mm	1.5
Angular frequency of the laser, rad s^{-1}	1.75×10^{15}
Permittivity, F m^{-1}	8.85×10^{-12}

Supplementary Table 9. Material properties of alloys used in dataset.

Parameter	AMS-nDB	AMS-mCB	IN738	AMSC-DB	AMS-OR
Solidus temperature, K	1598	1445	1400	1616	1586
Liquidus temperature, K	1717	1672	1625	1701	1699
Density, kg m^{-3}	8175	8646	8083	8113	8128
Thermal conductivity, W m^{-1} K^{-1}	15.03	11.39	17.87	18.34	18.57
Specific heat capacity, J kg^{-1} K^{-1}	518	547	574	599	602
Latent heat of fusion, kJ kg^{-1}	284.37	247.97	231.53	284.37	299.37
Dynamic viscosity, Pa s	5.23×10^{-3}	6.88×10^{-3}	7.02×10^{-3}	5.42×10^{-3}	5.47×10^{-3}
Surface tension, N m^{-1}	1.44	1.51	1.53	1.44	1.45

Here, ‘T’ represents temperature in K. Density is taken at room temperature, latent heat of fusion at the solidus temperature, and dynamic viscosity at the liquidus temperature. The temperature dependence of density, thermal conductivity, specific heat capacity, dynamic viscosity and surface tension are calculated using Thermo-Calc software and TCNI12 database.

Supplementary Note 17: Some perspectives on the proposed alloy design framework

The core of the current alloy design framework lies in the construction of the knowledge graph. Therefore, when extending the framework to other alloy systems or additive manufacturing techniques, it is necessary to introduce intermediate physical metallurgy information on top of the composition/process–property data. Such information may include atomic-scale mechanisms derived from first-principles calculations, thermodynamic and kinetic data obtained from methods such as Thermo-Calc, and solidification-related information simulated by finite element methods—domain knowledge that can directly or indirectly influence the predicted properties. These inputs must be adapted according to the specific alloy system (e.g., ultra-high-strength steels, titanium alloys) and the additive manufacturing technique (e.g., L-DED, L-PBF, E-PBF), with particular attention paid to the solidification characteristics of precipitate phases during the additive manufacturing process. The knowledge graph is then constructed based on hierarchical relationships among these variables.

Additionally, in the present work the knowledge graph was constructed solely on the basis of expert knowledge; the optimized construction of knowledge graphs remains a valuable direction for future research. Furthermore, the primary design focus of this work was placed on defect levels and room-temperature hardness. Future studies should aim at a comprehensive assessment of tensile or creep properties, considering both the as-printed and heat-treated conditions, which would expand the design space to include post-processing parameters, with the goal of designing alloys that exhibit superior overall performance.

Supplementary References

[1] Reed, R. C. *The superalloys: fundamentals and applications*. (Cambridge university press, 2008).

[2] Wei, H. L., Elmer, J. W. & DebRoy, T. Three-dimensional modeling of grain structure evolution during welding of an aluminum alloy. *Acta Mater.* **126**, 413-425 (2017).

[3] Martin, J. H. *et al.* 3D printing of high-strength aluminium alloys. *Nature* **549**, 365-369 (2017).

[4] DebRoy, T. *et al.* Additive manufacturing of metallic components – Process, structure and properties. *Prog. Mater. Sci.* **92**, 112-224 (2018).

[5] Mondal, B., Mukherjee, T. & DebRoy, T. Crack free metal printing using physics informed machine learning. *Acta Mater.* **226**, 117612 (2022).

[6] Tang, S., Ning, L. K., Xin, T. Z. & Zheng, Z. Coarsening Behavior of Gamma Prime Precipitates in a Nickel Based Single Crystal Superalloy. *J. Mater. Sci. Technol.* **32**, 172-176 (2016).

[7] White, R. J. The particle size distributions in systems evolving from interface-controlled to diffusion-controlled coarsening kinetics. *Materials Science and Engineering* **40**, 15-20 (1979).

[8] Liu, Y. *et al.* Predicting creep rupture life of Ni-based single crystal superalloys using divide-and-conquer approach based machine learning. *Acta Mater.* **195**, 454-467 (2020).

[9] Tang, Y. T. *et al.* Alloys-by-design: Application to new superalloys for additive manufacturing. *Acta Mater.* **202**, 417-436 (2021).

[10] Wang, C., Zhu, K., Hedström, P., Li, Y. & Xu, W. A generic and extensible model for the martensite start temperature incorporating thermodynamic data mining and deep learning framework. *J. Mater. Sci. Technol.* **128**, 31-43 (2022).

[11] Wei, X., van der Zwaag, S., Jia, Z., Wang, C. & Xu, W. On the use of transfer modeling to design new steels with excellent rotating bending fatigue resistance even in the case of very small calibration datasets. *Acta Mater.* **235**, 118103 (2022).

[12] Shen, C. *et al.* Physical metallurgy-guided machine learning and artificial intelligent design of ultrahigh-strength stainless steel. *Acta Mater.* **179**, 201-214 (2019).

[13] Jang, J. *et al.* Energy-Assisted additive manufacturing for weldable and non-weldable Ni-based superalloys: a review. *Virtual and Physical Prototyping* **20** (2025).

[14] Lu, Q., Xu, W. & van der Zwaag, S. The design of a compositionally robust martensitic creep-resistant steel with an optimized combination of precipitation hardening and solid-solution strengthening for high-temperature use. *Acta Mater.* **77**, 310-323 (2014).

[15] Bocklund, B., Bobbio, L. D., Otis, R. A., Beese, A. M. & Liu, Z.-K. Experimental validation of Scheil–Gulliver simulations for gradient path planning in additively manufactured functionally graded materials. *Materialia* **11** (2020).

[16] Yu, H., Liang, J., Bi, Z., Li, J. & Xu, W. Computational Design of Novel Ni Superalloys with Low Crack Susceptibility for Additive Manufacturing. *Metall. Mater. Trans. A* **53**, 1945-1954 (2022).

[17] Yu, H. *et al.* Robust additive manufacturable Ni superalloys designed by the integrated optimization of local elemental segregation and cracking susceptibility criteria. *Acta Mater.* **266** (2024).

[18] Kim, Y.-K. *et al.* A numerical model to predict mechanical properties of Ni-base disk superalloys. *Int. J.*

Plast. **110**, 123-144 (2018).
[19] Galindo-Nava, E. I., Connor, L. D. & Rae, C. M. F. On the prediction of the yield stress of unimodal and multimodal γ′ Nickel-base superalloys. *Acta Mater.* **98**, 377-390 (2015).
[20] Wang, Q. *et al.* A novel L12-strengthened single crystal high entropy alloy with excellent high-temperature mechanical properties. *Mater. Charact.* **212** (2024).
[21] Kim, Y.-K., Kim, D., Kim, H.-K., Oh, C.-S. & Lee, B.-J. An intermediate temperature creep model for Ni-based superalloys. *Int. J. Plast.* **79**, 153-175 (2016).
[22] Crudden, D. J., Mottura, A., Warnken, N., Raeisinia, B. & Reed, R. C. Modelling of the influence of alloy composition on flow stress in high-strength nickel-based superalloys. *Acta Mater.* **75**, 356-370 (2014).
[23] Kruml, T., Conforto, E., Piccolo, B. L., Caillard, D. & Martin, J. From dislocation cores to strength and work-hardening: a study of binary Ni3Al. *Acta Mater.* **50**, 5091-5101 (2002).
[24] Sundararajan, M., Taly, A. & Yan, Q. in *Proceedings of the 34th International Conference on Machine Learning* Vol. 70 (eds Precup Doina & Teh Yee Whye) 3319--3328 (PMLR, Proceedings of Machine Learning Research, 2017).
[25] Park, J.-U. *et al.* Alloy design of Ni-based superalloy with high γ′ volume fraction suitable for additive manufacturing and its deformation behavior. *Addit. Manuf.* **52** (2022).
[26] Pike, L. J. S. Development of a fabricable gamma-prime (γ′) strengthened superalloy. 191-200 (2008).
[27] Li, J., Wang, H. M. & Tang, H. B. Effect of heat treatment on microstructure and mechanical properties of laser melting deposited Ni-base superalloy Rene′41. *Mater. Sci. Eng. A.* **550**, 97-102 (2012).
[28] Wei, B., Ji, H. & Guo, J. Effect of heat treatments on the microstructure and mechanical properties of René 104 superalloy manufactured by selective laser melting. *Mater. Charact.* **200** (2023).
[29] Zou, T. *et al.* Effect of temperature on tensile behavior, fracture morphology, and deformation mechanisms of Nickel-based additive manufacturing 939 superalloy. *J. Alloy. Compd.* **959** (2023).
[30] Gruber, K., Dziedzic, R., Kuźnicka, B., Madejski, B. & Malicki, M. Impact of high temperature stress relieving on final properties of Inconel 718 processed by laser powder bed fusion. *Mater. Sci. Eng. A.* **813** (2021).
[31] Kanagarajah, P., Brenne, F., Niendorf, T. & Maier, H. J. Inconel 939 processed by selective laser melting: Effect of microstructure and temperature on the mechanical properties under static and cyclic loading. *Mater. Sci. Eng. A.* **588**, 188-195 (2013).
[32] Bauer, T., Dawson, K., Spierings, A. & Wegener, K. in *Proceedings of the 26th annual international solid freeform fabrication symposium.* 813-822 (2015).
[33] Kalyanasundaram, V. *et al.* Tensile and creep-rupture response of additively manufactured nickel-based superalloy CM247LC. *Addit. Manuf. Lett.* **5** (2023).
[34] Yang, C. *et al.* Microstructural evolution and high-temperature strengthening mechanisms of the IN 738LC superalloy prepared by selective laser melting. *J. Mater. Res. Technol.* **29**, 5304-5316 (2024).
[35] Murray, S. P. *et al.* A defect-resistant Co–Ni superalloy for 3D printing. *Nat. Commun.* **11** (2020).
[36] Smith, T. M. *et al.* The mechanisms underlying the enhanced high-temperature properties of GRX-810. *Nat Commun* **17**, 963 (2025).
[37] Yang, T. *et al.* Enhancement of mechanical properties of LDEDed IN738LC alloy by solid-solution

strengthening coupled with precipitation-strengthening. *J. Alloy. Compd.* **982** (2024).
[38] Shi, Y. *et al.* Effect of platform temperature on the porosity, microstructure and mechanical properties of an Al–Mg–Sc–Zr alloy fabricated by selective laser melting. *Mater. Sci. Eng. A.* **732**, 41-52 (2018).
[39] Shi, Y., Rometsch, P., Yang, K., Palm, F. & Wu, X. Characterisation of a novel Sc and Zr modified Al–Mg alloy fabricated by selective laser melting. *Mater. Lett.* **196**, 347-350 (2017).
[40] Tang, H. *et al.* Mechanical Properties of High Mg-Content Al-Mg-Sc-Zr Alloy Fabricated by Selective Laser Melting. *Met Mater Int* **27**, 2592-2599 (2021).
[41] Hyer, H. *et al.* Elimination of extraordinarily high cracking susceptibility of aluminum alloy fabricated by laser powder bed fusion. *J. Mater. Sci. Technol.* **103**, 50-58 (2022).
[42] Pekok, M. A., Setchi, R., Ryan, M., Han, Q. & Gu, D. Effect of process parameters on the microstructure and mechanical properties of AA2024 fabricated using selective laser melting. *Int. J. Adv. Manuf. Technol.* **112**, 175-192 (2020).
[43] Wang, X. J., Zhang, L. C., Fang, M. H. & Sercombe, T. B. The effect of atmosphere on the structure and properties of a selective laser melted Al–12Si alloy. *Mater. Sci. Eng. A.* **597**, 370-375 (2014).
[44] Bibili Nzengue, A. G., Mpofu, K., Mathe, N. R. & Muvunzi, R. Optimising a processing window for the production of aluminium silicon-12 samples via selective laser melting. *J. Mater. Res. Technol.* **28**, 1062-1073 (2024).
[45] Maamoun, A. H., Xue, Y. F., Elbestawi, M. A. & Veldhuis, S. C. Effect of Selective Laser Melting Process Parameters on the Quality of Al Alloy Parts: Powder Characterization, Density, Surface Roughness, and Dimensional Accuracy. *Materials* **11**, 2343 (2018).
[46] Praneeth, J., Venkatesh, S. & Sivarama Krishna, L. Process parameters influence on mechanical properties of AlSi10Mg by SLM. *Mater. Today Proc.* (2023).
[47] Teng, X. *et al.* Parameter optimization and microhardness experiment of AlSi10Mg alloy prepared by selective laser melting. *Mater. Res. Express.* **6**, 086592 (2019).
[48] Yang, F. *et al.* Developing a novel high-strength Al–Mg–Zn–Si alloy for laser powder bed fusion. *Mater. Sci. Eng. A.* **851**, 143636 (2022).
[49] Li, L. *et al.* Microstructures and tensile properties of a selective laser melted Al–Zn–Mg–Cu (Al7075) alloy by Si and Zr microalloying. *Mater. Sci. Eng. A.* **787**, 139492 (2020).
[50] Li, L. *et al.* Microstructures and mechanical properties of Si and Zr modified Al–Zn–Mg–Cu alloy-A comparison between selective laser melting and spark plasma sintering. *J. Alloy. Compd.* **821**, 153520 (2020).
[51] Otani, Y. & Sasaki, S. Effects of the addition of silicon to 7075 aluminum alloy on microstructure, mechanical properties, and selective laser melting processability. *Mater. Sci. Eng. A.* **777**, 139079 (2020).
[52] Deng, S. *et al.* Microstructure and mechanical properties of selective laser melted Al-Zn-Mg-Si-Sc-Zr alloy with high hot-cracking resistance. *J. Alloy. Compd.* **973**, 172930 (2024).
[53] Dreano, A. *et al.* Computational design of a crack-free aluminum alloy for additive manufacturing. *Addit. Manuf.* **55**, 102876 (2022).
[54] Zhu, Z. *et al.* Superior mechanical properties of a selective-laser-melted AlZnMgCuScZr alloy enabled by a tunable hierarchical microstructure and dual-nanoprecipitation. *Materials Today* **52**, 90-101 (2022).
[55] Croteau, J. R. *et al.* Microstructure and mechanical properties of Al-Mg-Zr alloys processed by selective

laser melting. *Acta Mater.* **153**, 35-44 (2018).
[56] Prashanth, K. G. *et al.* Microstructure and mechanical properties of Al–12Si produced by selective laser melting: Effect of heat treatment. *Mater. Sci. Eng. A.* **590**, 153-160 (2014).
[57] Hyer, H. *et al.* Composition-dependent solidification cracking of aluminum-silicon alloys during laser powder bed fusion. *Acta Mater.* **208** (2021).
[58] Xiong, Z. H. *et al.* Role of melt pool boundary condition in determining the mechanical properties of selective laser melting AlSi10Mg alloy. *Mater. Sci. Eng. A.* **740-741**, 148-156 (2019).
[59] Li, W. *et al.* Effect of heat treatment on AlSi10Mg alloy fabricated by selective laser melting: Microstructure evolution, mechanical properties and fracture mechanism. *Mater. Sci. Eng. A.* **663**, 116-125 (2016).
[60] Aboulkhair, N. T., Maskery, I., Tuck, C., Ashcroft, I. & Everitt, N. M. The microstructure and mechanical properties of selectively laser melted AlSi10Mg: The effect of a conventional T6-like heat treatment. *Mater. Sci. Eng. A.* **667**, 139-146 (2016).
[61] Wang, L., Jiang, X., Guo, M., Zhu, X. & Yan, B. Characterisation of structural properties for AlSi10Mg alloys fabricated by selective laser melting. *Mater Sci Tech-Lond* **33**, 2274-2282 (2017).
[62] Fousová, M., Dvorský, D., Michalcová, A. & Vojtěch, D. Changes in the microstructure and mechanical properties of additively manufactured AlSi10Mg alloy after exposure to elevated temperatures. *Mater. Charact.* **137**, 119-126 (2018).
[63] Rao, J. H. *et al.* The origins for tensile properties of selective laser melted aluminium alloy A357. *Addit. Manuf.* **17**, 113-122 (2017).
[64] Yang, K. V., Rometsch, P., Davies, C. H. J., Huang, A. & Wu, X. Effect of heat treatment on the microstructure and anisotropy in mechanical properties of A357 alloy produced by selective laser melting. *Mater. Des.* **154**, 275-290 (2018).
[65] Zhou, L. *et al.* Microstructure and tensile property of a novel AlZnMgScZr alloy additively manufactured by gas atomization and laser powder bed fusion. *Scr. Mater.* **158**, 24-28 (2019).
[66] Li, R. *et al.* Effect of aging treatment on the microstructure and mechanical properties of Al-3.02Mg-0.2Sc-0.1Zr alloy printed by selective laser melting. *Mater. Des.* **168**, 107668 (2019).
[67] Ma, R. *et al.* Effect of bimodal microstructure on the tensile properties of selective laser melt Al-Mg-Sc-Zr alloy. *J. Alloy. Compd.* **815**, 152422 (2020).
[68] Bi, J. *et al.* Densification, microstructure and mechanical properties of an Al-14.1Mg-0.47Si-0.31Sc-0.17Zr alloy printed by selective laser melting. *Mater. Sci. Eng. A.* **774**, 138931 (2020).
[69] Zhang, H. *et al.* Effect of Zirconium addition on crack, microstructure and mechanical behavior of selective laser melted Al-Cu-Mg alloy. *Scr. Mater.* **134**, 6-10 (2017).
[70] Zhang, H., Zhu, H., Qi, T., Hu, Z. & Zeng, X. Selective laser melting of high strength Al–Cu–Mg alloys: Processing, microstructure and mechanical properties. *Mater. Sci. Eng. A.* **656**, 47-54 (2016).
[71] Nie, X. *et al.* Effect of Zr content on formability, microstructure and mechanical properties of selective laser melted Zr modified Al-4.24Cu-1.97Mg-0.56Mn alloys. *J. Alloy. Compd.* **764**, 977-986 (2018).
[72] Hu, Z. *et al.* On the role of atmospheric oxygen into mechanical properties and fracture behavior of selective laser melted AlCu5MnCdVA. *Mater. Des.* **150**, 18-27 (2018).

[73] Lei, Z. *et al.* Effect of energy density on formability, microstructure and micro-hardness of selective laser melted Sc- and Zr- modified 7075 aluminum alloy. *Powder Technol.* **356**, 594-606 (2019).
[74] Mukherjee, T., Wei, H. L., De, A. & DebRoy, T. Heat and fluid flow in additive manufacturing – Part II: Powder bed fusion of stainless steel, and titanium, nickel and aluminum base alloys. *Comput. Mater. Sci.* **150**, 369-380 (2018).
[75] Mukherjee, T., Wei, H. L., De, A. & DebRoy, T. Heat and fluid flow in additive manufacturing—Part I: Modeling of powder bed fusion. *Comput. Mater. Sci.* **150**, 304-313 (2018).
[76] Collur, M. M., Paul, A. & DebRoy, T. Mechanism of alloying element vaporization during laser welding. *Metallurgical Transactions B* **18**, 733-740 (1987).
[77] Wirth, F. & Wegener, K. A physical modeling and predictive simulation of the laser cladding process. *Addit. Manuf.* **22**, 307-319 (2018).
[78] Voller, V. R. & Swaminathan, C. R. Eral Source-Based Method for Solidification Phase Change. *Numer. Heat Transf., Part B: Fundam.* **19**, 175-189 (1991).